



THE HONG KONG
POLYTECHNIC UNIVERSITY

香港理工大學

Pao Yue-kong Library

包玉剛圖書館

Copyright Undertaking

This thesis is protected by copyright, with all rights reserved.

By reading and using the thesis, the reader understands and agrees to the following terms:

1. The reader will abide by the rules and legal ordinances governing copyright regarding the use of the thesis.
2. The reader will use the thesis for the purpose of research or private study only and not for distribution or further reproduction or any other purpose.
3. The reader agrees to indemnify and hold the University harmless from and against any loss, damage, cost, liability or expenses arising from copyright infringement or unauthorized usage.

IMPORTANT

If you have reasons to believe that any materials in this thesis are deemed not suitable to be distributed in this form, or a copyright owner having difficulty with the material being included in our database, please contact lbsys@polyu.edu.hk providing details. The Library will look into your claim and consider taking remedial action upon receipt of the written requests.

Pao Yue-kong Library, The Hong Kong Polytechnic University, Hung Hom, Kowloon, Hong Kong

<http://www.lib.polyu.edu.hk>

**CROSS-MODAL VIBRATION ENERGY
METHOD FOR DYNAMIC FORCE
IDENTIFICATION**

MAO CHEN

**M.Phil
The Hong Kong
Polytechnic University
2014**

The Hong Kong Polytechnic University

Department of Mechanical Engineering

**Cross-Modal Vibration Energy
Method for Dynamic Force
Identification**

MAO Chen

**A thesis submitted in partial fulfilment of the
requirements for the degree of Master of Philosophy**

September 2013

CERTIFICATE OF ORIGINALITY

I hereby declare that this thesis is all of my own work and that, to the best of my knowledge and belief, it reproduces no material previously published or written, nor material that has been accepted for the award of any other degree or diploma, except where due acknowledgement has been made in the text.

_____ (Signed)

MAO Chen _____ (Name of student)

Abstract

Force identification is important in locating the vibration and noise sources of an operating machine. The forced vibration response of linearly vibrating structure is linear by definition. However, the energy distribution of linearly vibrating structures contains “coupled terms” in the modal decomposition of the response function. These coupled terms represent the cross-modal energy terms of a dynamic structure under forced vibration. In this research, it is proved analytically that certain cross-modal energy terms are highly correlated to the location of the external exciting force. Based on this finding, a new force localization method based on the cross-modal energy terms is developed, and a new index based on the suitably selected cross-modal energy terms to locate the force is developed. Numerical tests on beam structures under force excitation with different frequencies and locations have been carried out to test the effectiveness of the proposed force localization method. It is found that the proposed force localization method works well on vibrating beam structures even when random noise is taken into consideration. It is shown that the new method can identify the exciting force well. Experiments are done for verification of the proposed force localization method.

Acknowledgements

I would like to express my greatest appreciation to Dr. W.O. Wong, my chief-supervisor, for his guidance, suggestions and encouragement throughout my research work. I also sincerely thank him for giving me the opportunity to start my research.

I am indebted to Prof. L. Cheng, my co-supervisor, for his suggestions and permission to use the resources for preparing my thesis.

My gratitude should also go to Y.L. Cheung and H. Xu, for their kind advice and instruction. Lastly, thank all my friend mates.

Table of Contents

Abstract.....	i
Acknowledgements.....	ii
List of Tables.....	v
List of Figures.....	vi
Nomenclature.....	ix
Chapter 1 Introduction.....	1
1.1 Review of force identification methods.....	1
1.2 Energy decomposition and research motivation.....	4
1.3 Methodology and arrangement of the following chapters.....	6
Chapter 2 Energy Decomposition and Force Localization Index for Cross-Modal Energy Method.....	9
2.1 Decomposition of vibration energy.....	10
2.1.1 Vibration energy of Euler-Bernoulli Beam.....	10
2.1.2 Decomposition of energy.....	13
2.1.3 Physical meaning of energy decomposition.....	16
2.2 Force Localization Index.....	19
2.2.1 Accumulation phenomenon of cross-modal energy term.....	20
2.2.2 Definition of force localization index.....	30
2.3 Summary.....	30
Chapter 3 Numerical Solution for Energy Decomposition and Force Localization Index.....	32
3.1 Numerical solution for energy decomposition.....	32
3.2 Numerical solution for force localization index.....	34
3.3 Summary.....	42
Chapter 4 Experiment of Cross-Modal Energy Method.....	43
4.1 Inverse problem in experiment.....	43
4.2 Numerical experiment.....	45

4.3	Experimental test of the cross-modal energy method.....	59
4.3.1	Experimental set-up.....	59
4.3.2	Results of experiment.....	63
4.4	Summary.....	73
Chapter 5 Conclusions and Suggestions for Future Work.....		75
5.1	Conclusions.....	75
5.2	Limitations and suggestions for future work.....	76
Appendix A.....		77
References.....		78

List of Tables		page
Table 2.1	Boundary conditions and coefficient relationship	22
Table 3.1	Natural frequencies obtained in numerical solution (pin-pin boundary condition)	36
Table 3.2	Natural frequencies obtained in numerical solution (fixed-free boundary condition)	39
Table 4.1	Extracted and theoretical modal ratio coefficients (pin-pin boundary condition)	47
Table 4.2	Extracted and theoretical modal ratio coefficients (fixed-free boundary condition)	50
Table 4.3	Measured natural frequencies with theoretical values	65
Table 4.4	Modal ratio coefficients in experimental test	69
Table 4.5	Normalized modal ratio coefficients in experimental test, numerical experiment and numerical solution (fixed-free boundary condition)	70

List of Figures	page
Figure 1.1 Methodology and arrangement of chapters	8
Figure 2.1 Illustration of the procedure of energy decomposition and extraction of FLI	9
Figure 2.2 Illustration of a beam excited by a concentrated force	11
Figure 2.3 Values of trigonometric and hyperbolic components along the beam (pin-free/fixed boundary condition)	25
Figure 2.4 Values of trigonometric and hyperbolic components along the beam (free/fixed-free/fixed boundary conditions)	28
Figure 3.1 Illustration of the procedure of energy decomposition and extraction of FLI (pin-pin boundary condition, $x_f = 0.35L$)	33
Figure 3.2 Accumulation phenomenon in FLI (pin-pin boundary condition, $x_f = 0.35L$, $\omega_f = 600\pi$ rad/s, $F_0 = 500$ N and $\alpha = 0$)	35
Figure 3.3 FLI under different driving frequencies of exciting force (pin-pin boundary condition, $x_f = 0.35L$, $F_0 = 500$ N, $\alpha = 0$ and $n = 7$)	36
Figure 3.4 FLI under different locations of exciting force (pin-pin boundary condition, $\omega_f = 600\pi$ rad/s, $F_0 = 500$ N, $\alpha = 0$ and $n = 7$)	37

Figure 3.5	Accumulation phenomenon in FLI (fixed-free boundary condition, $x_f = 0.35L$, $\omega_f = 300\pi$ rad/s, $F_0 = 500$ N and $\alpha = 1$)	38
Figure 4.1	Displacement response with 3% random noise (pin-pin boundary condition)	46
Figure 4.2	Mode shapes with 3% random noise (pin-pin boundary condition)	47
Figure 4.3	FLI calculated in numerical experiment (pin-pin boundary condition, $x_f = 0.35L$, $\omega_f = 600\pi$ rad/s, $F_0 = 500$ N and $\alpha = 0$)	48
Figure 4.4	Displacement response with 3% random noise (fixed-free boundary condition)	49
Figure 4.5	Mode shapes with 3% random noise (fixed-free boundary condition)	50
Figure 4.6	FLI calculated in numerical experiment (fixed-free boundary condition, $x_f = 0.35L$, $\omega_f = 300\pi$ rad/s, $F_0 = 500$ N and $\alpha = 1$)	51
Figure 4.7	Displacement response with 30% random noise (pin-pin boundary condition)	53
Figure 4.8	FLI calculated with 30% random noise (pin-pin boundary condition, $x_f = 0.35L$, $\omega_f = 600\pi$ rad/s, $F_0 = 500$ N and $\alpha = 0$)	53
Figure 4.9	Displacement response with 30% random noise (fixed-free boundary condition)	54

Figure 4.10	FLI calculated with 30% random noise (fixed-free boundary condition, $x_f = 0.35L$, $\omega_f = 300 \pi$ rad/s, $F_0 = 500$ N and $\alpha = 1$)	54
Figure 4.11	FLI calculated with 30% random noise after reducing the noise amplified by derivative (pin-pin boundary condition, $x_f = 0.35L$, $\omega_f = 600 \pi$ rad/s, $F_0 = 500$ N and $\alpha = 0$)	55
Figure 4.12	FLI calculated with 30% random noise after reducing the noise amplified by derivative (pin-pin boundary condition, $x_f = 0.35L$, $\omega_f = 300 \pi$ rad/s, $F_0 = 500$ N and $\alpha = 0$)	55
Figure 4.13	Influence of noise on cross-modal energy method	58
Figure 4.14	Set-up of experimental test	60
Figure 4.15	Measurement procedures in experimental test	62
Figure 4.16	Point mobility FRF using white noise	64
Figure 4.17	Mass-normalized measured and theoretical mode shapes	68
Figure 4.18	Measured operational velocity response	69
Figure 4.19	FLI calculated in experimental test (fixed-free boundary condition $x_f = 0.35L$, $\omega_f = 300 \pi$ rad/s and $\alpha = 1$)	71
Figure 4.20	FLI calculated in experimental test after noise reduction (fixed-free boundary condition, $x_f = 0.35L$, $\omega_f = 300 \pi$ rad/s and $\alpha = 1$)	71

Nomenclature

Most of the symbols used in this thesis have been defined in the text. The following list includes some of the more important symbols and those that have not been defined explicitly in the text.

$e(x,t)$ Energy density of a beam

$E(x)$ Mean energy density of a beam

$E_{jk}(x)$ Modal energy density element

The definition of $E_{jk}(x)$ is

$$E_{jk}(x) = \frac{1}{2} \cdot \left(\frac{1}{2} m \cdot \omega_f^2 \cdot W_j(x) \cdot W_k(x) + \frac{1}{2} YI \cdot \frac{d^2(W_j(x))}{dx^2} \cdot \frac{d^2(W_k(x))}{dx^2} \right)$$

When $j = k = r$, $E_{rr}(x)$ is the Diagonal-modal energy density element. When $j \neq k$, $E_{jk}(x)$ is the Cross-modal energy density element.

$E_{\text{Dia}}(x)$ Diagonal-modal energy density

The definition of $E_{\text{Dia}}(x)$ is $E_{\text{Dia}}(x) = \sum_{r=1}^{\infty} E_{rr}(x) \cdot \eta_r^2$

$E_{\text{Cro}}(x)$ Cross-modal energy density

The definition of $E_{\text{Cro}}(x)$ is $E_{\text{Cro}}(x) = \sum_{\substack{j=1 \\ j \neq k}}^{\infty} \sum_{\substack{k=1 \\ k \neq j}}^{\infty} E_{jk}(x) \cdot \eta_j \eta_k$

$E_{\text{Cro_High}}(x)$ The high order terms of cross-modal energy density

The definition of $E_{\text{Cro_High}}(x)$ is

$$E_{\text{Cro_High}}(x) = \sum_{\substack{j=r+\alpha \\ j \neq k}}^n \sum_{\substack{k=r+\alpha \\ k \neq j}}^n \eta_j \cdot \eta_k \cdot E_{jk}(x) = \sum_{\substack{j=r+\alpha \\ j \neq k}}^n \sum_{\substack{k=r+\alpha \\ k \neq j}}^n \Gamma_{jk} \cdot E_{jk}(x)$$

$E_{\text{Cro_High}}(x)$ is also the Force localization index.

$EN(t)$ Total vibration energy of a beam

$f(x,t)$ External exciting force

F_0 Magnitude of the external exciting force

$I(x)$ Moment of inertia

L Length of beam

$L(x)$ Mean Lagrangian energy density of a beam

$m(x)$ Mass per unit length

$T(t)$ Kinetic energy of a beam

$V(t)$ Potential energy of a beam

$w(x,t)$ Transverse displacement of a beam

$W_r(x)$ The r^{th} mode shape

x_f Location of the external exciting force

Y Young's modulus

Greek Letters

η_r The r^{th} modal ratio coefficient

The definition of η_r is

$$\eta_r = \frac{\int_0^L W_r(x) F_0 \delta(x - x_f) dx}{\omega_r^2 - \omega_f^2}$$

Γ_{jk} Amplification coefficient

The definition of Γ_{jk} is

$$\begin{aligned} \Gamma_{jk} &= \eta_j \eta_k \\ &= F_0^2 \cdot \frac{1}{\omega_j^2 - \omega_f^2} \cdot \frac{1}{\omega_k^2 - \omega_f^2} \cdot W_j(x_f) \cdot W_k(x_f) \end{aligned}$$

ω_f Driving frequency of the external exciting force

ω_r The r^{th} natural frequency

Subscripts

f External exciting force

j The j^{th} mode

k The k^{th} mode

r The r^{th} mode

Abbreviations

CMSE	Cross-modal strain energy
FAT	Force analysis technique
FRF	Frequency response function
LSM	Least squares method
ODS	Operational Detection Shape
SVD	Singular Value Decomposition

Chapter 1 Introduction

This chapter begins with a review of the literatures on force identification methods and energy decomposition. The research motivation is then established based on the review. A methodology to conduct the research is described.

1.1 Review of force identification methods

Force identification is of great importance in locating the vibration and noise source of an operating machine. A large number of studies have been conducted about indirect determination of the dynamic loadings [1, 7, 11, 23]. One typical method calculates the forces through Frequency Response Function (FRF) matrix and structural operational response as an inverse problem. Stevens [33] concluded the ill-conditioned problem occurred in force identification. Dobson and Rider [5] summarized different techniques used in the FRF matrix method and some applications. The method has been developed as a standard identification method [28], and applied to characterization of structure-borne sound sources [14, 15].

In order to solve the ill-conditioned problem involved in inverse problem of force identification, several studies have been conducted on improving the Least Squares Method (LSM), which was applied to solve the inverse problem. Karlsson [17] pointed out that spatial derivative in the inverse

problem amplifies the noise and makes the problem ill-conditioned. He further showed this amplification is closely related to FRF matrix, and can be improved by increasing the orthogonality between each columns of coefficient matrix. In order to improve the coefficient matrix, several studies were conducted in Singular Value Decomposition (SVD) [2, 32]. Fierro et al. [8] further introduced the truncated total least squares method and Liu et al. [21] analyzed the effect of applying regularization filter for SVD. Truncated singular value decomposition (TSVD) filter and the Tikhonov filter were studied in their work.

In order to avoid measuring FRF matrix, a new force identification method, Force Analysis Technique (FAT), was proposed by Pezerat and Guyader [27]. This method directly calculates the external exciting force from operational response through vibration governing equation. It is possible to deal with different types of excitations, including point forces [18, 30], moments [31] and even turbulent boundary layer excitation [19]. It has been applied to beams [27, 31], plates [28, 29] and shells [3, 4]. This method is built on the vibration governing equation for general boundary condition. And, this makes FAT could be applied without knowing the exact boundary condition [29].

Another approach using power flow, which has the similar advantage of

avoiding the calculation of FRF matrix, was applied to identify the force. Gavric and Pavic [10] initially presented the numerical calculation of power flow to indicate the vibration energy source and sinker based on the calculation method introduced by Noiseux [24] and Pavic [25]. The location of force is shown by the energy source. Gavirc et al. [9] conducted the experimental measurement to validate the method. It has been tested on some simple structures [10, 40] and even with some attempts on complex structures [9, 12]. The exact boundary condition can also be unknown in this method [39, 40].

However, there are two major problems of both FAT and power flow method. The first one is that non-uniform structure can contaminate the detection of the force identification index in FAT and power flow pattern in power flow method. The local variation of the structure in mass and stiffness can also be designated as a force in FAT [38]. For the power flow method, the complexity of the structure can complicate the pattern of power flow and therefore make it difficult to locate the energy source [12, 20].

The other one is that both methods utilize the derivative to extract the information of exciting force from the high order derivative of measured signal. The noise may be amplified by the derivative operation, and

therefore, the accuracy may be questioned. A regularization approach named “RIFF” was applied to FAT by Pezerat and Guyader as an improvement of the original method [28, 29]. This approach requires spatial windowing and wavenumber filtering to reduce the noise. The cut-off wavenumber of filter needs to be chosen carefully. About the power flow method, similarly, Zhang and Mann III [39, 40] also applied a two-dimensional Hanning window in spatial domain and an oval filter in wavenumber domain to the measured operational response. In 2006, Wang et al. [35] utilized B-spline approximation to reduce the noise in power flow measurement. Similarly, the cut-off wavenumber in these methods require to be chosen carefully to avoid filtering out the information of force.

1.2 Energy decomposition and research motivation

Based on the review of force identification methods, it can be found there are still two difficulties in the recently-developed methods: (1) the contamination of force identification index caused by non-uniform structure and (2) amplification of noise in the high order derivative of the vibration signal. Therefore, it is necessary to research a better method for locating the exciting force.

Energy can be a possible choice for the improvement. As shown in the

power flow method [10], the vibration energy of a structure is related to the exciting force. In that method, the information of force is shown by the change of energy flow pattern, which is extracted through high order derivative. However, there is another way to show the information related to the change of energy distribution caused by exciting force, and that is *to decompose the energy, separate the effect on energy distribution of exciting force from that of modal information of the structure and extract the part associated with the exciting force to form an index for force location*. The index will be defined in Section 2.2.2.

For energy decomposition, there are some literatures related to this topic, but few provides the insight about the physical meaning. In the studies of Kadambe, Boudreaux-Bartels [16] and Pei and Tsai [26], it is shown that cross elements, which are termed “cross terms”, arise naturally in time-frequency representations in signal analysis due to the non-linearity. Hu et al. [13] developed a Cross-Modal Strain Energy (CMSE) method to estimate damage. However, in their work, the CMSE does not represent a real mechanical energy but just an artificial term combining analytical and measured values. Therefore, its physical meaning is not clear.

Wang et al [36] and Wong et al [37] proposed a concept of “modal power flow” to identify the damage. In their papers, the energy was decomposed

based on the vibration modes under free vibration. However, the energy decomposition under forced vibration is not discussed.

Thus, the motivation of this research is to: (1) derive the modal decomposition of vibration energy and explore its physical meaning for Euler–Bernoulli beam; (2) develop the Force Localization Index (FLI) by using the decomposed energy terms related to the exciting harmonic force; and (3) verify the proposed FLI by computer simulations and experiments.

1.3 Methodology and arrangement of the following chapters

According to the three objectives proposed in Section 1.2, the research methodology is arranged into three parts: theory, simulation and experiment.

The work aims to derive the new force localization method based on the decomposition of vibration energy and explain the physical meaning of the decomposition according to the derivation. In the theory part, the decomposition of vibration energy was illustrated. The vibration energy was first divided into static part and dynamic part. Then, the static part was further divided into diagonal part and cross part. The definition of each part will be illustrated in Chapter 2. After the energy decomposition, the FLI was proposed based on the cross part of static energy. The application of

proposed FLI was also studied. Since this is a preliminary study, in order to focus on the basic concept, only uniform Euler-Bernoulli beam with light damping excited by one concentrated force is adopted as the model for examination. The boundary conditions discussed in this research are confined to common standard boundary conditions.

The simulation consists of Numerical Solution and Numerical Experiment. Numerical solution was calculated based on the theory in Chapter 2 for illustration of the theoretical prediction. Numerical experiment was conducted based on the experimental condition to study the effect of noise on the proposed method.

Experimental test was conducted after the numerical experiment in order to validate the proposed method. The procedure of experimental test is the same as that of numerical experiment, except that the displacement response and mode shapes were obtained by measurement not by simulation.

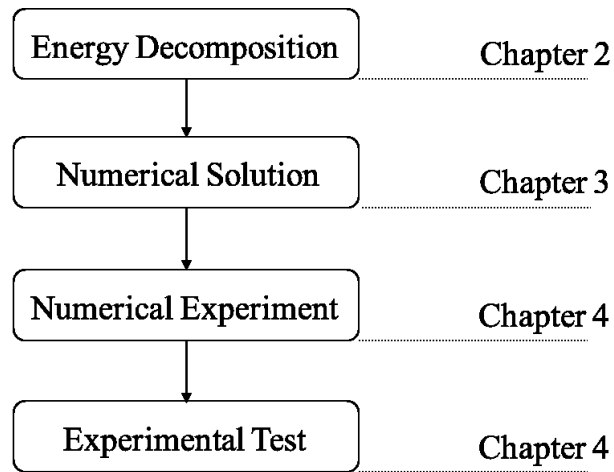


Figure 1.1 Methodology and arrangement of chapters

The following chapters are arranged accordingly to fulfill the motivation through the methodology as shown in Fig. 1.1. Chapter 2 contains the description of energy decomposition and discussion of the physical meaning to achieve motivation (1). The FLI is developed based on the energy decomposition to fulfill motivation (2). Motivation (3) is answered by Chapter 3 and Chapter 4. Chapter 3 shows the numerical solution; Chapter 4 contains the numerical experiment and the experimental test. Chapter 5 summaries the findings in this research. Then, the significance and limitations are discussed. Based on the discussions, some suggestions for future works are provided.

Chapter 2 Energy Decomposition and Force Localization

Index for Cross-Modal Energy Method

This chapter shows the derivation of FLI by decomposition of vibration energy for Euler-Bernoulli beam. The vibration energy decomposition is first illustrated. The physical meaning of decomposition is discussed. Then, based on the energy decomposition, the FLI is defined by the discovery of the accumulation phenomenon. Fig. 2.1 illustrates the outline of the procedure of energy decomposition and derivation of FLI.

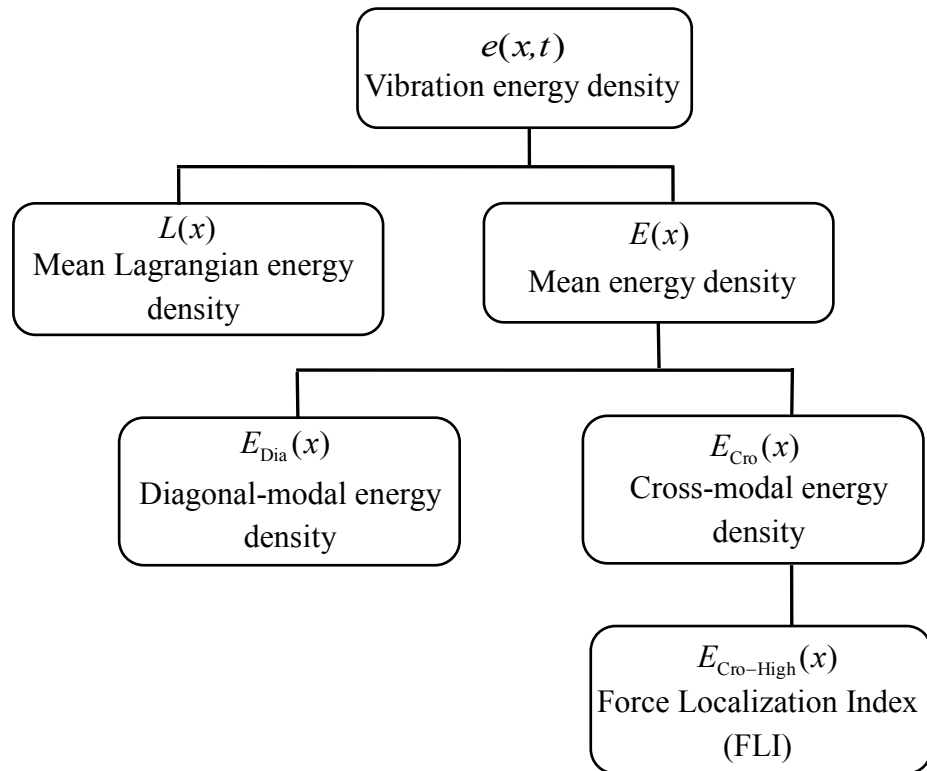


Figure 2.1 Illustration of the procedure of energy decomposition and extraction of FLI

2.1 Decomposition of vibration energy

In this section, the decomposition of vibration energy for Euler-Bernoulli beam is illustrated, and the physical meaning of decomposition is discussed.

2.1.1 Vibration energy of Euler-Bernoulli Beam

For Euler-Bernoulli beam, the partial differential equation for free bending vibration is [22]

$$m(x)\frac{\partial^2 w(x,t)}{\partial t^2} + \frac{\partial^2}{\partial x^2} \left[YI(x)\frac{\partial^2 w(x,t)}{\partial x^2} \right] = 0, \quad 0 < x < L \quad (2.1)$$

where $w(x,t)$ is the transverse displacement, $m(x)$ the mass per unit length, $YI(x)$ the flexural rigidity, in which Y is the Young's modulus and $I(x)$ the cross-sectional area moment of inertia about an axis passing through the center of the cross section, and L the length of beam.

The mode shape can be described by a general solution written as

$$W_r(x) = A \sin(\beta_r x) + B \cos(\beta_r x) + C \sinh(\beta_r x) + D \cosh(\beta_r x) \quad (2.2)$$

where $W_r(x)$ is the r^{th} mode shape; A , B , C and D are constants to be determined by boundary conditions. And, β_r is determined by

$$\beta_r^4 = \frac{\omega_r^2 m}{YI} \quad (2.3)$$

where ω_r is the r^{th} natural frequency.

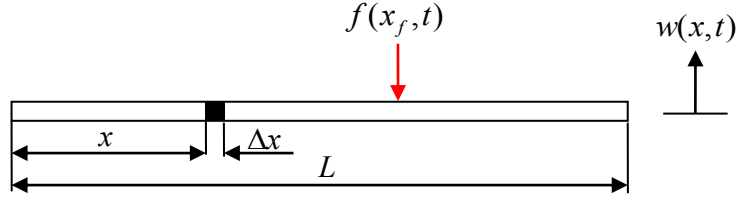


Figure 2.2 Illustration of a beam excited by a concentrated force

When a concentrated external harmonic force is applied on the beam, as shown in Fig. 2.2, the partial differential equation is changed to

$$\begin{aligned} m(x) \frac{\partial^2 w(x, t)}{\partial t^2} + \frac{\partial^2}{\partial x^2} \left[YI(x) \frac{\partial^2 w(x, t)}{\partial x^2} \right] &= f(x, t) \\ &= F_0 \delta(x - x_f) \sin(\omega_f t), \quad 0 < x < L \end{aligned} \quad (2.4)$$

where $f(x, t)$ is the external exciting force, F_0 the magnitude of the force, x_f the location of the force and ω_f the driving frequency of the force.

Assuming the excitation is a concentrated harmonic force, the displacement of the beam under such applied force, which is the solution for Eq. (2.4),

may be written as

$$w(x,t) = \sum_{r=1}^{\infty} \eta_r \cdot W_r(x) \cdot \sin(\omega_f t) \quad (2.5)$$

where η_r is the r^{th} modal ratio coefficient and defined by

$$\eta_r = \frac{\int_0^L W_r(x) F_0 \delta(x - x_f) dx}{\omega_r^2 - \omega_f^2} \quad (2.6)$$

The vibration energy of the beam can be written in terms of the displacement as [22]

$$\begin{aligned} EN(t) &= T(t) + V(t) \\ &= \frac{1}{2} \int_0^L m(x) \left[\frac{\partial w(x,t)}{\partial t} \right]^2 dx + \frac{1}{2} \int_0^L YI(x) \left[\frac{\partial^2 w(x,t)}{\partial x^2} \right]^2 dx \end{aligned} \quad (2.7)$$

where $EN(t)$ is the total energy of beam, $T(t)$ the kinetic energy and $V(t)$ the potential energy. Thus, the total energy of the beam under forced vibration can be acquired by substituting Eq. (2.5) into Eq. (2.7).

However, when considering force localization, it is of great advantage to know the local information of energy rather than the global one. In order to obtain the local description of the energy, the energy density $e(x,t)$ is defined

$$e(x,t) = \lim_{\Delta x \rightarrow 0} \frac{\Delta E(x,t)}{\Delta x} = \frac{1}{2} m(x) \cdot \dot{w}(x,t)^2 + \frac{1}{2} YI(x) \cdot \left[\frac{\partial^2 w(x,t)}{\partial x^2} \right]^2 \quad (2.8)$$

where Δx is the length of an infinitesimal element, as shown in Fig. 2.2, and $\Delta E(x,t)$ is the instantaneous energy of that element

$$\begin{aligned}\Delta E(x,t) &= \Delta T(x,t) + \Delta V(x,t) \\ &= \frac{1}{2} m(x) \cdot \Delta x \cdot \dot{w}(x,t)^2 + \frac{1}{2} YI(x) \cdot \left[\frac{\partial^2 w(x,t)}{\partial x^2} \right]^2 \cdot \Delta x\end{aligned}\quad (2.9)$$

Thus, the energy distribution along the beam is determined by energy density. By substituting Eq. (2.5) into Eq. (2.8), the energy distribution under forced vibration is obtained.

2.1.2 Decomposition of energy

The vibration energy of the beam can be treated as the summation of kinetic energy and potential energy, as shown by Eq. (2.7), and it can also be represented by a combination of static and dynamic components written as

$$\begin{aligned}e(x,t) &= \frac{1}{2} m(x) \cdot \dot{w}(x,t)^2 + \frac{1}{2} YI(x) \cdot \left[\frac{\partial^2 w(x,t)}{\partial x^2} \right]^2 \\ &= \frac{1}{2} m(x) \cdot \left(\sum_{r=1}^{\infty} \omega_f \cdot \eta_r \cdot W_r(x) \cdot \cos(\omega_f t) \right)^2 + \frac{1}{2} YI(x) \cdot \left(\sum_{r=1}^{\infty} \eta_r \cdot \frac{\partial^2 W_r(x)}{\partial x^2} \cdot \sin(\omega_f t) \right)^2 \\ &= \frac{1}{2} \left(\frac{1}{2} m(x) \cdot \omega_f^2 \cdot \left(\sum_{r=1}^{\infty} \eta_r \cdot W_r(x) \right)^2 + \frac{1}{2} YI(x) \cdot \left(\sum_{r=1}^{\infty} \eta_r \cdot \frac{\partial^2 W_r(x)}{\partial x^2} \right)^2 \right) \\ &\quad + \frac{1}{2} \left(\frac{1}{2} m(x) \cdot \omega_f^2 \cdot \left(\sum_{r=1}^{\infty} \eta_r \cdot W_r(x) \right)^2 - \frac{1}{2} YI(x) \cdot \left(\sum_{r=1}^{\infty} \eta_r \cdot \frac{\partial^2 W_r(x)}{\partial x^2} \right)^2 \right) \cdot \cos(2\omega_f t) \\ &= E(x) + L(x) \cdot \cos(2\omega_f t)\end{aligned}\quad (2.10)$$

where

$$E(x) = \frac{1}{2} \left(\frac{1}{2} m(x) \cdot \omega_f^2 \cdot \left(\sum_{r=1}^{\infty} \eta_r \cdot W_r(x) \right)^2 + \frac{1}{2} YI(x) \cdot \left(\sum_{r=1}^{\infty} \eta_r \cdot \frac{\partial^2 W_r(x)}{\partial x^2} \right)^2 \right) \quad (2.11)$$

$$L(x) = \frac{1}{2} \left(\frac{1}{2} m(x) \cdot \omega_f^2 \cdot \left(\sum_{r=1}^{\infty} \eta_r \cdot W_r(x) \right)^2 - \frac{1}{2} YI(x) \cdot \left(\sum_{r=1}^{\infty} \eta_r \cdot \frac{\partial^2 W_r(x)}{\partial x^2} \right)^2 \right) \quad (2.12)$$

According to Eq. (2.10), the static part $E(x)$ is the mean energy density, whose integration along the beam is the total energy of beam. The amplitude of dynamic part $L(x)$ is the mean Lagrangian energy density [36].

After decomposing the vibration energy density into static and dynamic parts, the mean energy density can be further decomposed through the modal decomposition of displacement.

$$\begin{aligned} E(x) &= \sum_{j=1}^{\infty} \sum_{k=1}^{\infty} \frac{1}{2} \cdot \left(\frac{1}{2} m \cdot \omega_f^2 \cdot W_j(x) \cdot W_k(x) + \frac{1}{2} YI \cdot \frac{d^2(W_j(x))}{dx^2} \cdot \frac{d^2(W_k(x))}{dx^2} \right) \cdot \eta_j \cdot \eta_k \\ &= \sum_{j=1}^{\infty} \sum_{k=1}^{\infty} E_{jk}(x) \cdot \eta_j \eta_k \\ &= [\eta_1, \eta_2, \dots, \eta_n, \dots] \cdot \begin{bmatrix} E_{11}(x) & \cdots & E_{1n}(x) & \cdots \\ \vdots & \ddots & \vdots & \\ E_{n1}(x) & \cdots & E_{nn}(x) & \cdots \\ \vdots & & \vdots & \ddots \end{bmatrix} \cdot \begin{bmatrix} \eta_1 \\ \eta_2 \\ \vdots \\ \eta_n \\ \vdots \end{bmatrix} \end{aligned}$$

$$\begin{aligned}
&= \sum_{r=1}^{\infty} E_{rr}(x) \cdot \Gamma_{rr} + \sum_{\substack{j=1 \\ j \neq k}}^{\infty} \sum_{\substack{k=1 \\ k \neq j}}^{\infty} E_{jk}(x) \cdot \Gamma_{jk} \\
&= \sum_{r=1}^{\infty} E_{rr}(x) \cdot \eta_r^2 + \sum_{\substack{j=1 \\ j \neq k}}^{\infty} \sum_{\substack{k=1 \\ k \neq j}}^{\infty} E_{jk}(x) \cdot \eta_j \eta_k \\
&= E_{\text{Dia}}(x) + E_{\text{Cro}}(x)
\end{aligned} \tag{2.13}$$

where

$$E_{jk}(x) = \frac{1}{2} \cdot \left(\frac{1}{2} m \cdot \omega_f^2 \cdot W_j(x) \cdot W_k(x) + \frac{1}{2} YI \cdot \frac{d^2(W_j(x))}{dx^2} \cdot \frac{d^2(W_k(x))}{dx^2} \right) \tag{2.14}$$

and

$$\begin{aligned}
\Gamma_{jk} &= \eta_j \eta_k \\
&= \frac{\int_0^L W_j(x) F(x) dx}{\omega_j^2 - \omega_f^2} \cdot \frac{\int_0^L W_k(x) F(x) dx}{\omega_k^2 - \omega_f^2} \\
&= \frac{F_0}{\omega_j^2 - \omega_f^2} \cdot \int_0^L W_j(x) \delta(x - x_f) dx \cdot \frac{F_0}{\omega_k^2 - \omega_f^2} \cdot \int_0^L W_k(x) \delta(x - x_f) dx \\
&= F_0^2 \cdot \frac{1}{\omega_j^2 - \omega_f^2} \cdot \frac{1}{\omega_k^2 - \omega_f^2} \cdot W_j(x_f) \cdot W_k(x_f)
\end{aligned} \tag{2.15}$$

$E_{jk}(x)$ and Γ_{jk} are named as Modal Energy Density Element and Amplification Coefficient, respectively. $\Gamma_{jk} \cdot E_{jk}(x)$ is named as Modal Energy Term.

In Eq. (2.13), the mean energy density is divided into two parts. According to the position in matrix, the sum of all the diagonal-modal energy density

elements is named as diagonal-modal energy density $E_{\text{Dia}}(x)$. And, the sum of all the cross-modal energy density elements is named as cross-modal energy density $E_{\text{Cro}}(x)$.

2.1.3 Physical meaning of energy decomposition

In Eq. (2.13), static energy density is decomposed into diagonal-modal energy density and cross-modal energy density. This division separates the effect of exciting force on energy distribution from that of the structure.

The integration of mean energy density can be written as

$$\begin{aligned}
& \int_0^L E(x) \cdot dx \\
&= \int_0^L E_{\text{Dia}}(x) \cdot dx + \int_0^L E_{\text{Cro}}(x) \cdot dx \\
&= \int_0^L \sum_{r=1}^{\infty} E_{rr}(x) \cdot \Gamma_{rr} \cdot dx + \int_0^L \sum_{\substack{j=1 \\ j \neq k}}^{\infty} \sum_{\substack{k=1 \\ k \neq j}}^{\infty} E_{jk}(x) \cdot \Gamma_{jk} \cdot dx \\
&= \sum_{r=1}^{\infty} \int_0^L E_{rr}(x) \cdot \Gamma_{rr} \cdot dx + \sum_{\substack{j=1 \\ j \neq k}}^{\infty} \sum_{\substack{k=1 \\ k \neq j}}^{\infty} \int_0^L E_{jk}(x) \cdot \Gamma_{jk} \cdot dx \tag{2.16}
\end{aligned}$$

The total energy of the beam is composed of the integration of diagonal-modal energy density and cross-modal energy density. Since diagonal-modal energy density element $E_{rr}(x)$ is positive, the integration of $E_{rr}(x)$ is positive.

$$\int_0^L E_{rr}(x) dx > 0, \quad r = 1 \cdots n \cdots \tag{2.17}$$

For cross-modal energy density element $E_{jk}(x)$, $j \neq k$, however, can be negative. It is important to notice that the integration of cross-modal energy density element is zero under the normal boundary conditions, including pin, fixed and free end. This is proved as follows.

The normal boundary conditions make the system self-adjoint [34], and therefore, if the mode shapes are mass-normalized, the alternative companion orthonormality relations can be written as [22]

$$\int_0^L YI(x) \cdot \frac{d^2(W_j(x))}{dx^2} \cdot \frac{d^2(W_k(x))}{dx^2} \cdot dx = \delta_{jk}, \quad j, k = 1, \dots, n, \dots \quad (2.18)$$

The orthonormality relations is

$$\int_0^L m(x) \cdot W_j(x) \cdot W_k(x) \cdot dx = \delta_{jk}, \quad j, k = 1, \dots, n, \dots \quad (2.19)$$

Using Eq. (2.18) and Eq. (2.19), the integration of cross-modal energy density element over the beam is

$$\int_0^L E_{jk}(x) \cdot dx = 0, \quad j \neq k; j, k = 1, \dots, n, \dots \quad (2.20)$$

Based on Eq. (2.16), Eq. (2.17) and Eq. (2.20), the explanation of physical meaning can be provided in the following.

(a) The physical meaning of diagonal-modal energy density element

According to Eq. (2.14), diagonal-modal energy density element $E_{rr}(x)$ shows the modal energy distribution based originally on the characteristic of structure, which is its mode shape. The integration of diagonal-modal energy density element means the total energy, which comes from external exciting force, stored in that mode.

(b) The physical meaning of cross-modal energy density element

Different from diagonal-modal energy density element, it is necessary to give a reasonable explanation for the negative energy shown in cross element. Since the integration of cross-modal energy density element over the beam is zero as shown in Eq. (2.20), which means that there is no energy gain or loss of the system, it probably means that energy is moved from negative place to the positive one inside the system. And so, the cross-modal energy density element $E_{jk}(x)$ represents an energy shift or redistribution associated with j^{th} and k^{th} modal energy density.

(c) The physical meaning of diagonal-modal energy density

According to Eq. (2.13), diagonal-modal energy density $E_{\text{Dia}}(x)$ is the sum of all diagonal-modal energy terms. $E_{\text{Dia}}(x)$ represents the total energy stored inside the structure and its original distribution based on its mode shapes.

(d) The physical meaning of cross-modal energy density

Cross-modal energy density $E_{Cro}(x)$ is the sum of all cross-modal energy terms. $E_{Cro}(x)$ represents the total energy shift caused by external exciting force that redistributes the modal energy distribution.

In summary, the vibration energy density was decomposed into static part and dynamic part. Then, the static part of vibration energy was further divided into diagonal-modal energy density and cross-modal energy density. And, the decomposition of static energy by utilizing diagonal and cross-modal energy density may separate the effect of external exciting force on energy distribution from the original energy distribution based on the structure itself.

According to Eq. (2.13), it could be found that this shift is related to Γ_{jk} , and from Eq. (2.15), Γ_{jk} is related to the location and driving frequency of exciting force. Therefore, $E_{Cro}(x)$ may be capable to show the location of exciting force.

2.2 Force Localization Index

In Section 2.1, the cross-modal energy density was extracted from mean energy density by decomposition. And, the cross-modal energy density shows the energy shift caused by exciting force. In this Section, an accumulation phenomenon of cross-modal energy term at the location of

exciting force is discovered in the high order terms of cross-modal energy density. Based on the discovery of accumulation phenomenon, the FLI is defined.

2.2.1 Accumulation phenomenon of cross-modal energy term

Based on Eq. (2.15), the cross-modal energy term can be written as

$$\begin{aligned}
& \Gamma_{jk} \cdot E_{jk}(x) \\
&= F_0^2 \cdot \frac{1}{\omega_j^2 - \omega_f^2} \cdot \frac{1}{\omega_k^2 - \omega_f^2} \cdot W_j(x_f) \cdot W_k(x_f) \\
&\cdot \frac{1}{2} \left(\frac{1}{2} m(x) \cdot \omega_f^2 \cdot W_j(x) \cdot W_k(x) + \frac{1}{2} YI(x) \cdot \frac{d^2(W_j(x))}{dx^2} \cdot \frac{d^2(W_k(x))}{dx^2} \right), \quad j \neq k.
\end{aligned} \tag{2.21}$$

It can be found that the value of $\Gamma_{jk} \cdot E_{jk}(x)$ in Eq. (2.21) is decided by the location x and the order of modes j and k . With the change of the order of mode, this value is uncertain, and thus can be positive or negative. However, at the location of exciting force x_f , $\Gamma_{jk} \cdot E_{jk}(x)$ can be written as

$$\begin{aligned}
& \Gamma_{jk} \cdot E_{jk}(x_f) \\
&= \frac{F_0^2}{4(\omega_j^2 - \omega_f^2) \cdot (\omega_k^2 - \omega_f^2)} \cdot \left(m(x) \cdot \omega_f^2 \cdot W_j(x_f)^2 \cdot W_k(x_f)^2 \right. \\
&\quad \left. + YI(x) \cdot W_j(x_f) \cdot W_k(x_f) \cdot \frac{d^2(W_j(x_f))}{dx^2} \cdot \frac{d^2(W_k(x_f))}{dx^2} \right), \quad j \neq k \tag{2.22}
\end{aligned}$$

It can be found that if just high order terms are considered, where $\omega_i > \omega_f, \omega_r > \omega_f$, the part before parenthesis in Eq. (2.22) is positive.

The first component in parenthesis is also positive. So, the sign of $\Gamma_{jk} \cdot E_{jk}(x_f)$ depends on the second component in parenthesis. Since

the terms with subscript j or k have same structure, it is necessary just

to consider component $W_r(x_f) \cdot \frac{d^2(W_r(x_f))}{dx^2}$ to determine the sign of

high order cross-modal energy term at the location of exciting force.

Since the location of exciting force x_f can be any position along the beam, the symbol x_f is substituted by x , which does not affect the result,

in the following analysis. To investigate the sign of $W_r(x) \cdot \frac{d^2(W_r(x))}{dx^2}$,

results are enumerated under all the combinations of common general

boundary conditions (pin, fixed and free). By substituting the general

solution of mode shape, Eq. (2.2), the component can be written as

$$W_r(x) \cdot \frac{d^2(W_r(x))}{dx^2} = -\beta_r^2 \left((A \sin(\beta_r x) + B \cos(\beta_r x))^2 - (C \sinh(\beta_r x) + D \cosh(\beta_r x))^2 \right) \quad (2.23)$$

Some of the relationships between coefficients in Eq. (2.23) can be determined through the boundary condition at the location $x=0$, as shown in Table 2.1.

It can be found that the coefficient relationships of fixed end and free end obtain the same result when the relationships shown in Table 2.1 are substituted into Eq. (2.23). So, there are just two groups of boundary conditions need to consider: pin end and fixed/free end. Since the change of sides does not affect the boundary condition, just half of the combinations (pin-pin, pin-free/fixed and free/fixed-free/fixed) are under consideration in the following analysis.

Table 2.1 Boundary conditions and coefficient relationship

Boundary condition	Mathematics description	Coefficient relationship
Pin end	$w _{x=0} = 0$	$B + D = 0$
	$\frac{\partial^2 w}{\partial x^2} \Big _{x=0} = 0$	$-B + D = 0$
Fixed end	$w _{x=0} = 0$	$B + D = 0$
	$\frac{\partial w}{\partial x} \Big _{x=0} = 0$	$A + C = 0$
Free end	$\frac{\partial^2 w}{\partial x^2} \Big _{x=0} = 0$	$-B + D = 0$
	$\frac{\partial^3 w}{\partial x^3} \Big _{x=0} = 0$	$-A + C = 0$

(a) Pin-pin and pin-free/fixed boundary conditions

Since there is pin end at $x=0$, the value of B and D can be determined, and that is $B = D = 0$. Eq. (2.23) is simplified as

$$W_r(x) \cdot \frac{d^2(W_r(x))}{dx^2} = -\beta_r^2 A^2 \left(\sin^2(\beta_r x) - \frac{C^2}{A^2} \sinh^2(\beta_r x) \right) \quad (2.24)$$

For pin-pin boundary condition, the pin end at $x=L$ results in $C=0$.

Therefore, the sign of $W_r(x) \cdot \frac{d^2(W_r(x))}{dx^2}$ is determined by trigonometric component $-\sin^2(\beta_r x)$ in Eq. (2.24), which is always be negative.

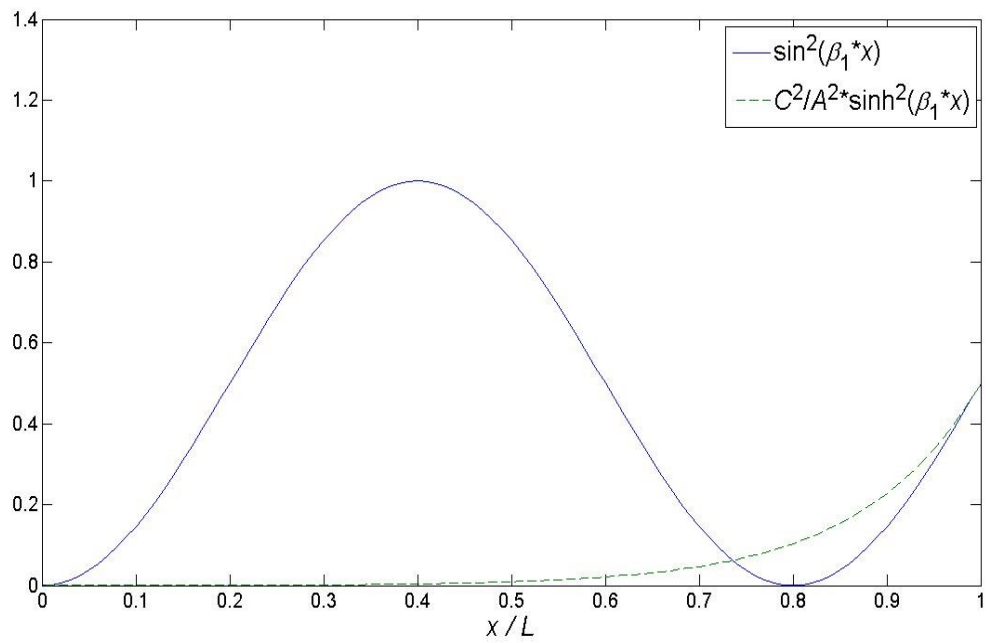
For pin-free/fixed boundary condition, the hyperbolic component $\sinh^2(\beta_r x)$ also has effect on the sign. The free/fixed end results in the coefficient relationship

$$\frac{C^2}{A^2} = \frac{\sin^2(\beta_r L)}{\sinh^2(\beta_r L)} \quad (2.25)$$

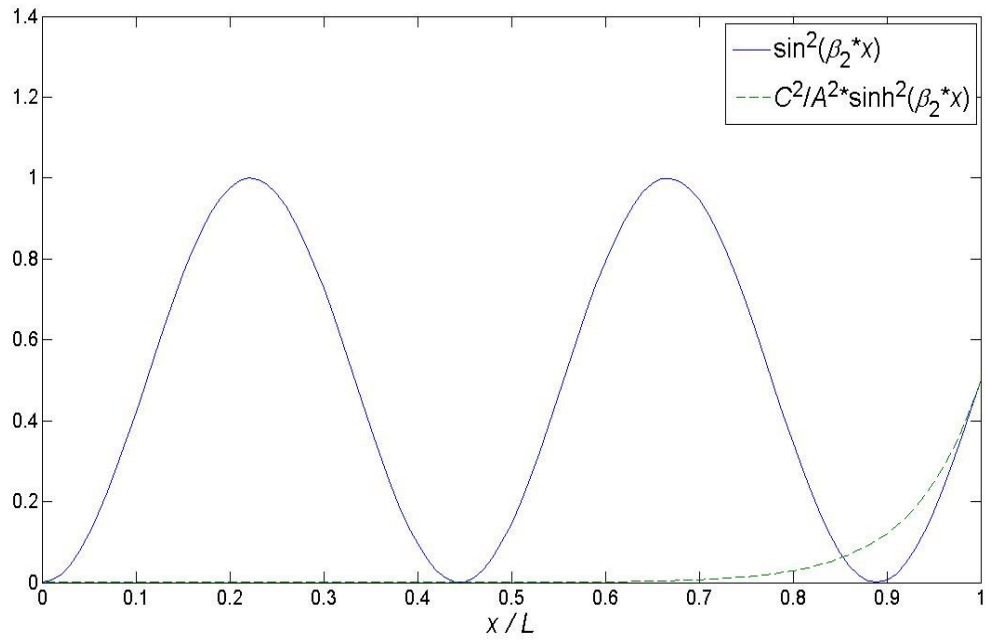
The values of trigonometric and hyperbolic components in Eq. (2.24) along the beam is shown in Fig. 2.3, when the order of mode r is increasing.

It can be found that the hyperbolic component makes $W_r(x) \cdot \frac{d^2(W_r(x))}{dx^2}$ positive at the region right to the intersection point. However, with the increase of the order of mode r , the positive region caused by the

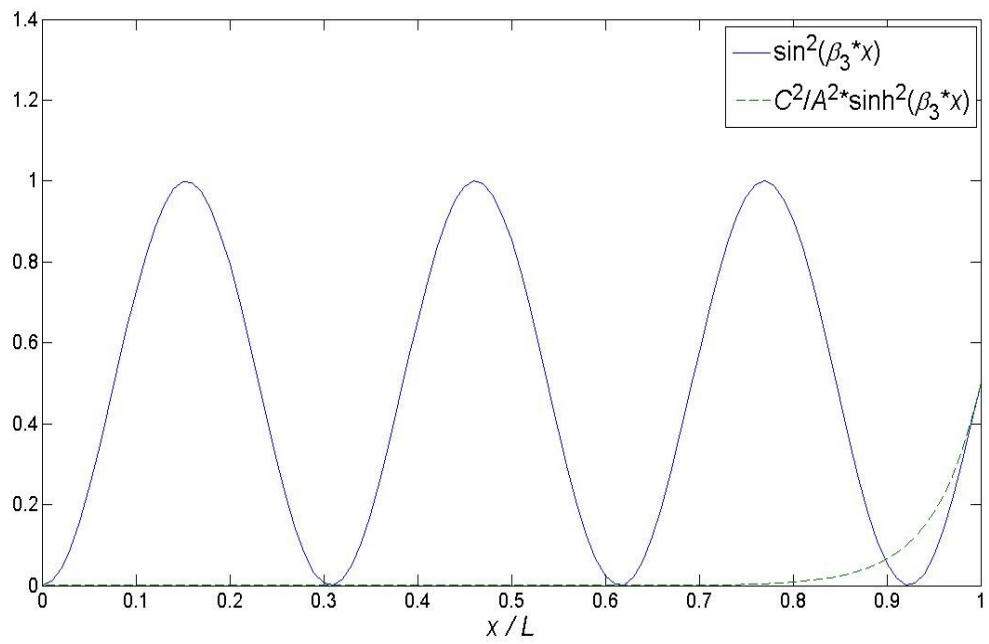
hyperbolic component is gradually shifted to the free/fixed end. This means when considering high order modes, the effect of the boundary condition can be neglected when the position is enough far away from the free/fixed end.



(a) $r = 1$



(b) $r = 2$



(c) $r = 3$

Figure 2.3 Values of trigonometric and hyperbolic components along the beam (pin-free/fixed boundary condition)

(b) Free/fixed-free/fixed boundary conditions

For the free/fixed end at $x = 0$, the relationships between coefficients can be determined, and those are $B = -D$ $A = -C$ or $B = D$ $A = C$. Eq.

(2.23) can be simplified as

$$\begin{aligned}
 & W_r(x) \cdot \frac{d^2(W_r(x))}{dx^2} \\
 &= -\beta_r^2 A^2 \left(\left(\sin(\beta_r x) + \frac{B}{A} \cos(\beta_r x) \right)^2 - \left(\sinh(\beta_r x) + \frac{B}{A} \cosh(\beta_r x) \right)^2 \right)
 \end{aligned}
 \tag{2.26}$$

For free/fixed-free/fixed boundary condition, the hyperbolic component

$\left(\sinh(\beta_r x) + \frac{B}{A} \cosh(\beta_r x) \right)^2$ also has effect on the sign. The free/fixed end

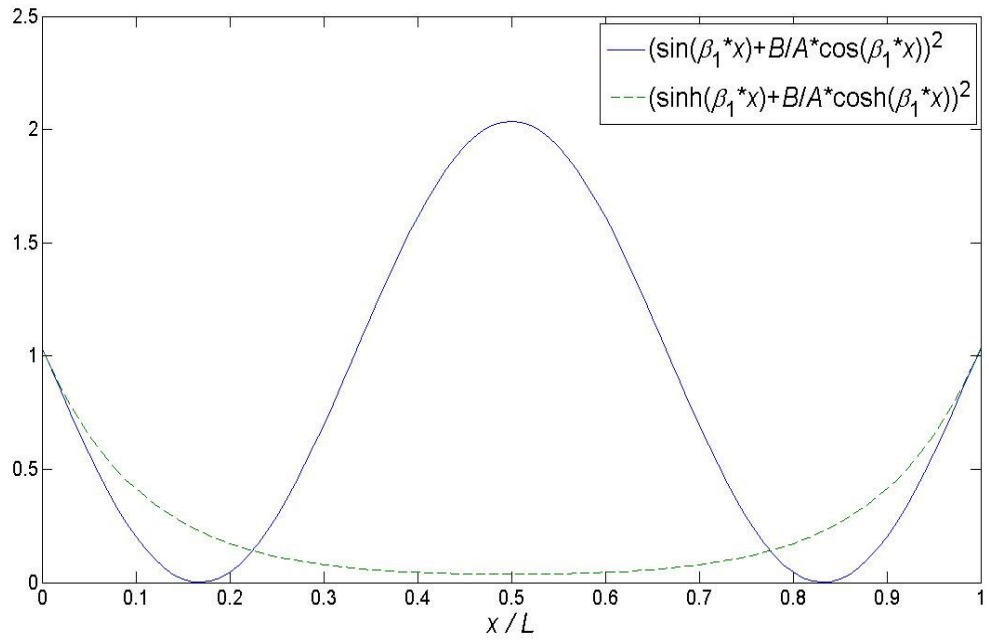
results in the coefficient relationship

$$\frac{B}{A} = \frac{\sin(\beta_r L) - \sinh(\beta_r L)}{\cos(\beta_r L) - \cosh(\beta_r L)}
 \tag{2.27}$$

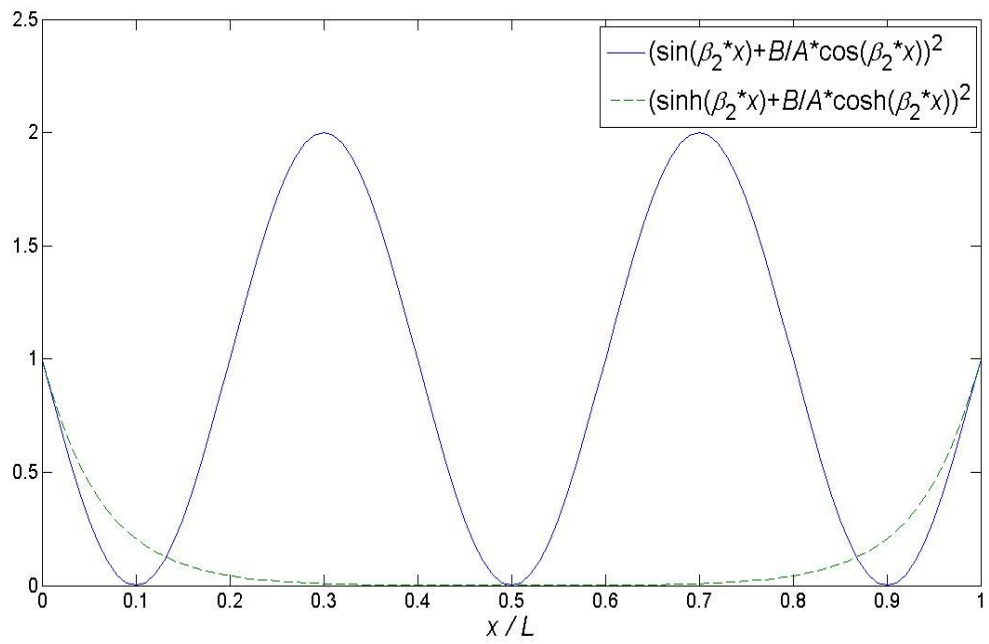
The values of both of the trigonometric and hyperbolic components in

Eq. (2.26) along the beam is shown in Fig. 2.4, when the order of

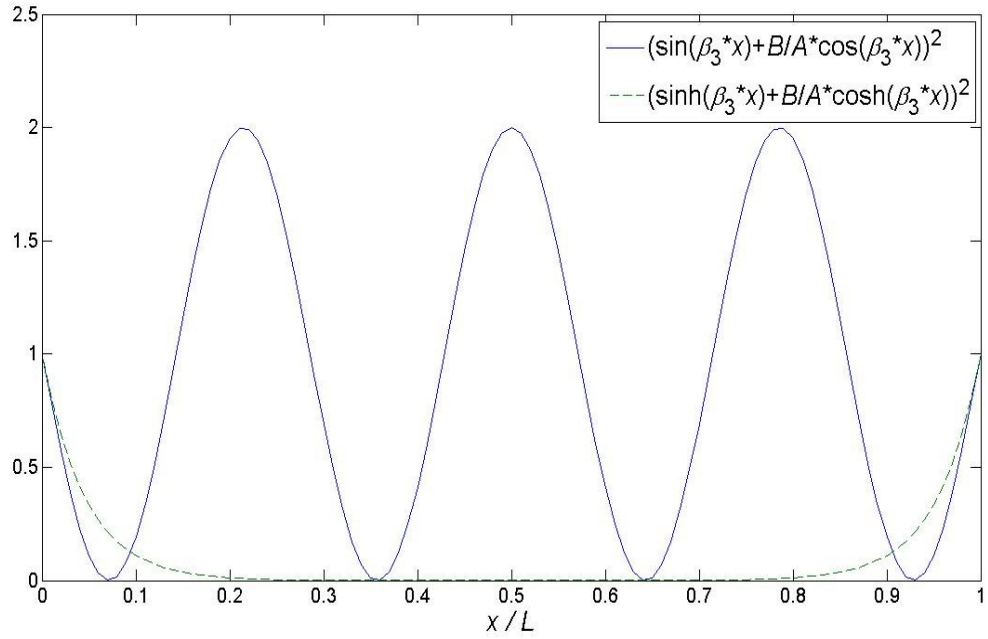
mode r is increasing.



(a) $r = 1$



(b) $r = 2$



(c) $r = 3$

Figure 2.4 Values of trigonometric and hyperbolic components along the beam (free/fixed-free/fixed boundary conditions)

Like the results in pin-free/fixed boundary condition, the effect of hyperbolic component caused by free/fixed end just affects the region near the boundary. With the increase of order, the region is becoming closer to the boundary. This means when considering high order modes, the sign of

$$W_r(x) \cdot \frac{d^2(W_r(x))}{dx^2} \text{ can be consider as negative when the position is enough}$$

far away from the free/fixed end.

To sum up, according to the results shown under all possible boundary conditions, it can be conclude that for high order modes, when x is

enough far away from boundary, $W_r(x) \cdot \frac{d^2(W_r(x))}{dx^2}$ is negative. This

means that when the location of exciting force x_f is enough far away

from boundary, the component $W_r(x_f) \cdot \frac{d^2(W_r(x_f))}{dx^2}$ is always negative.

Thus, the second component in parenthesis in Eq. (2.22) is always positive.

This means that cross-modal energy term $\Gamma_{jk} \cdot E_{jk}(x_f)$ is always positive

under some conditions, which can be described as

$$\Gamma_{jk} \cdot E_{jk}(x_f) \geq 0, \quad j \neq k \quad (2.28)$$

when $\omega_i > \omega_f, \omega_r > \omega_f$ and x_f is enough far away from the

boundary.

Therefore, the value of cross-modal energy term $\Gamma_{jk} \cdot E_{jk}(x)$ is positive at

the location of exciting force under some conditions, while at other

locations the sign of this value is uncertain. By adding increasing number

of high order cross-modal energy terms, at the position x_f , the value of the

summation is becoming larger, since the sign of each cross-modal energy

term is positive at this position. However, at other positions, the values of

high order cross-modal energy term are changed with the order. This means

that after adding another high order cross-modal energy term, the value of

summation may increase or decrease. Therefore, only at the location of

exciting force, the value of summation of high order cross-modal energy

terms is always increasing. This phenomenon results in the accumulation phenomenon of the summation of high order cross-modal energy terms at the location of exciting when the number of the terms in summation is increasing.

2.2.2 Definition of force localization index

On the basis of the accumulation phenomenon of the summation of high order cross-modal energy terms at the location of exciting force, the FLI is defined by utilizing the summation of just high order cross-modal energy terms.

$$E_{\text{Cro-High}}(x) = \sum_{\substack{j=r+\alpha \\ j \neq k}}^n \sum_{\substack{k=r+\alpha \\ k \neq j}}^n \eta_j \cdot \eta_k \cdot E_{jk}(x) = \sum_{\substack{j=r+\alpha \\ j \neq k}}^n \sum_{\substack{k=r+\alpha \\ k \neq j}}^n \Gamma_{jk} \cdot E_{jk}(x) \quad (2.29)$$

where $\omega_{r-1} < \omega_f < \omega_r$; α and n control the number of high order cross-modal energy terms in the FLI. $E_{\text{Cro-High}}(x)$ is named as the high order terms of cross-modal energy density, respectively.

2.3 Summary

Section 2.1 illustrated the decomposition of vibration energy for Euler-Bernoulli beam, and the cross-modal energy density was obtained by the decomposition. The cross-modal energy density may have the physical meaning to show the energy shift caused by exciting force. Section 2.2 showed the discovery of the accumulation phenomenon of the summation

of high order cross-modal energy terms at the location of exciting force.

Based on this phenomenon, the FLI was defined accordingly.

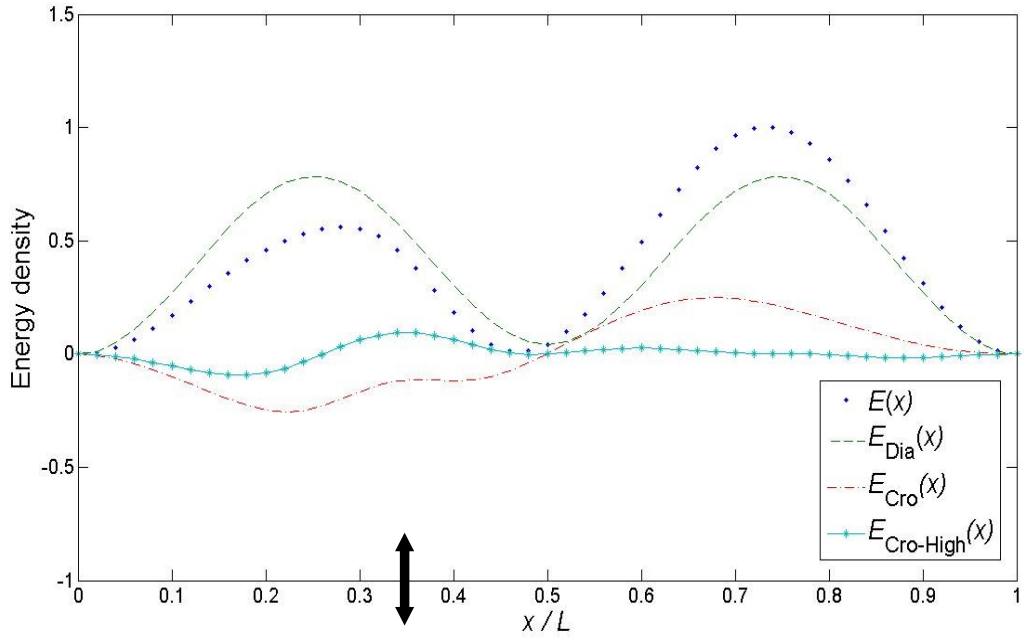
Chapter 3 Numerical Solution for Energy Decomposition and Force Localization Index

Chapter 3 contains the numerical solution for energy decomposition and FLI to illustrate the theoretical prediction shown in previous chapter.

3.1 Numerical solution for energy decomposition

In Chapter 2, the static part of vibration energy was decomposed into diagonal and cross-modal energy density. The FLI was obtained by further extracting the high order terms of cross-modal energy density. In order to illustrate this procedure of energy decomposition and extraction of location information of exciting force by this energy decomposition, a numerical solution is calculated as follows.

A mild steel beam with rectangular cross section was modeled to simulate the beam. The length of it is $L = 0.3$ m. The height and the width of the beam are $h = 0.0047$ m and $b = 0.0191$ m. The density and Young's modulus were assumed to be $\rho = 7740$ kg/m³ and $Y = 204$ GPa. The external exciting force was applied on a pin-pin supported beam at $x_f = 0.35L$. The simulation was calculated in software *Matlab*. The calculated mean energy density, diagonal-modal energy density, cross-modal energy density and high order terms of cross-modal energy density are plotted in Fig. 3.1.



* This figure is normalized through division by the maximum value.

Figure 3.1 Illustration of the procedure of energy decomposition and extraction of FLI (pin-pin boundary condition, $x_f = 0.35L$)

In Fig. 3.1, it can be found that it is difficult to find the location of force directly from the mean energy density $E(x)$. After decomposition, as discussed in Section 2.1.3, the diagonal-modal energy density $E_{\text{Dia}}(x)$ represents the energy distribution based on the modal information of the structure, and the cross-modal energy density $E_{\text{Cro}}(x)$ shows the energy shift caused by external exciting force. By further decomposition, the FLI, high order terms of cross-modal energy density $E_{\text{Cro-High}}(x)$, is extracted and shows the peak at the location of exciting force, and therefore indicates the location of force.

3.2 Numerical solution for force localization index

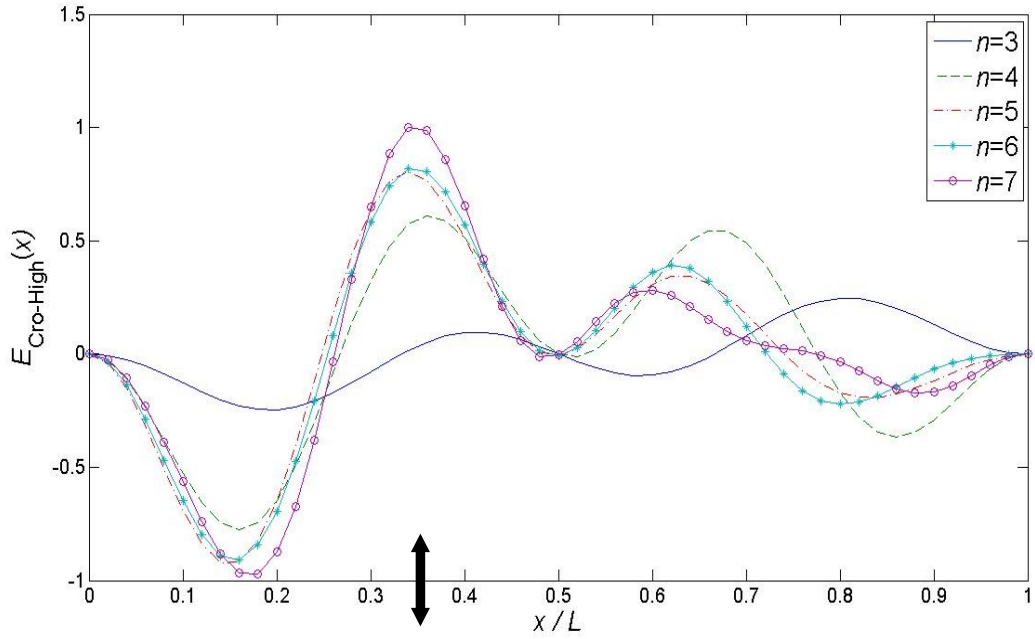
In Section 2.2, it was discovered that an accumulation phenomenon of the summation of high order cross-modal energy terms could occur at the location of exciting force in FLI. In order to illustrate this predicted accumulation phenomenon, a numerical solution is calculated as follows. The beam model utilized in this section is the same as the one in Section 3.1. In this simulation, both pin-pin and fixed-free boundary conditions were calculated. And, excitations with different locations and driving frequencies were applied on the beam. The parameter n , which controls the number of high order cross-modal energy terms in FLI, was increasing in some simulation to show the accumulation phenomenon. The FLI was calculated based on the theory (Eq. (2.21) and Eq. (2.29)).

The driving frequency was chosen not close to the natural frequencies. This is because that structure usually is designed to vibrate at the frequency away from its natural frequencies. This can also avoid ill-condition in LSM so that the preliminary issues can be focused on. The results of numerical solution for FLI under pin-pin boundary condition are shown in Fig. 3.2, Fig. 3.3 and Fig. 3.4.

(a) Accumulation phenomenon in FLI

The external exciting force was applied at $x_f = 0.35L$ with driving

frequency $\omega_f = 600\pi$ rad/s. The parameter α in Eq. (2.29) was 0, and n was increased from 3 to 7. The magnitude of exciting force F_0 was 500 N in all the cases of numerical solution. The interval between two sample points was $0.01L$ through the numerical solution.



* This figure is normalized through division by the maximum value.

Figure 3.2 Accumulation phenomenon in FLI (pin-pin boundary condition, $x_f = 0.35L$, $\omega_f = 600\pi$ rad/s, $F_0 = 500$ N and $\alpha = 0$)

(b) FLI under different driving frequencies of exciting force

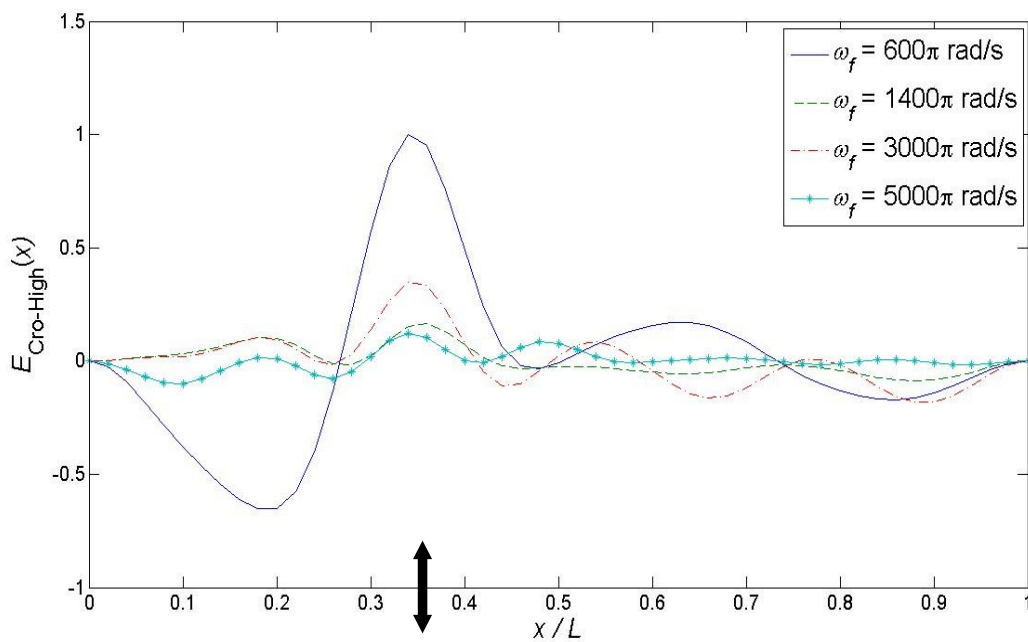
The exciting force was applied at $x_f = 0.35L$ and $\alpha = 0$, $n = 7$. The driving frequency ω_f changed across different natural frequencies. The natural frequencies are shown in Table 3.1. The FLI under different driving frequencies of exciting force are shown in Fig. 3.3.

(c) FLI under different locations of exciting force

The driving frequency of exciting force was $\omega_f = 600\pi$ rad/s and $\alpha = 0$, $n = 7$. The location of exciting force varied along the beam. The FLI under different locations of exciting force are shown in Fig. 3.4.

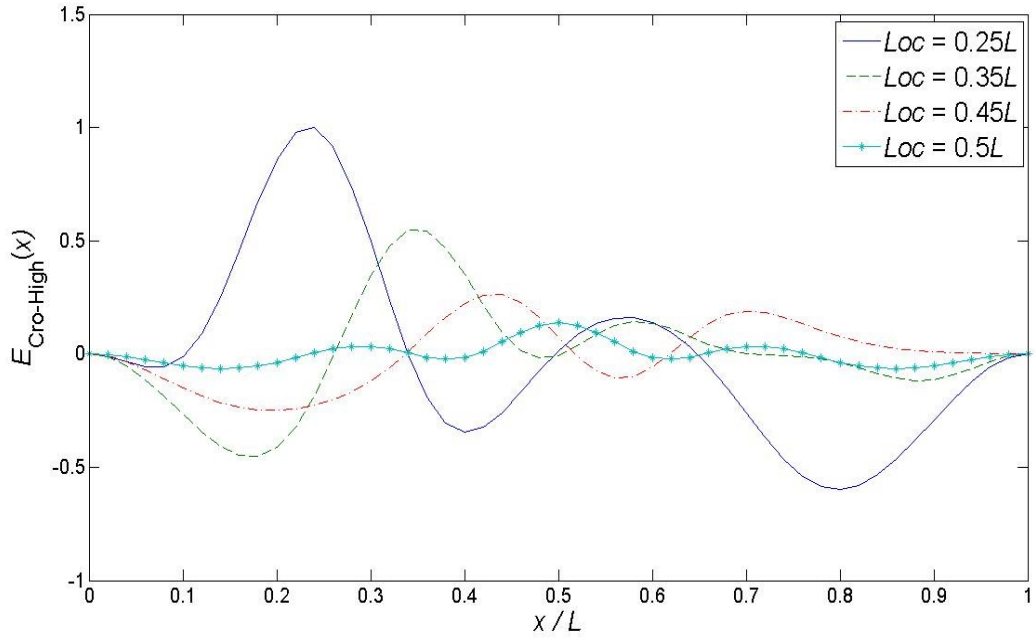
Table 3.1 Natural frequencies obtained in numerical solution (pin-pin boundary condition)

	1 st	2 nd	3 rd	4 th
Natural frequency (rad/s)	243π	972π	2188π	3890π
	5 th	6 th	7 th	
	6078π	8753π	11914π	



* This figure is normalized through division by the maximum value.

Figure 3.3 FLI under different driving frequencies of exciting force (pin-pin boundary condition, $x_f = 0.35L$, $F_0 = 500$ N, $\alpha = 0$ and $n = 7$)



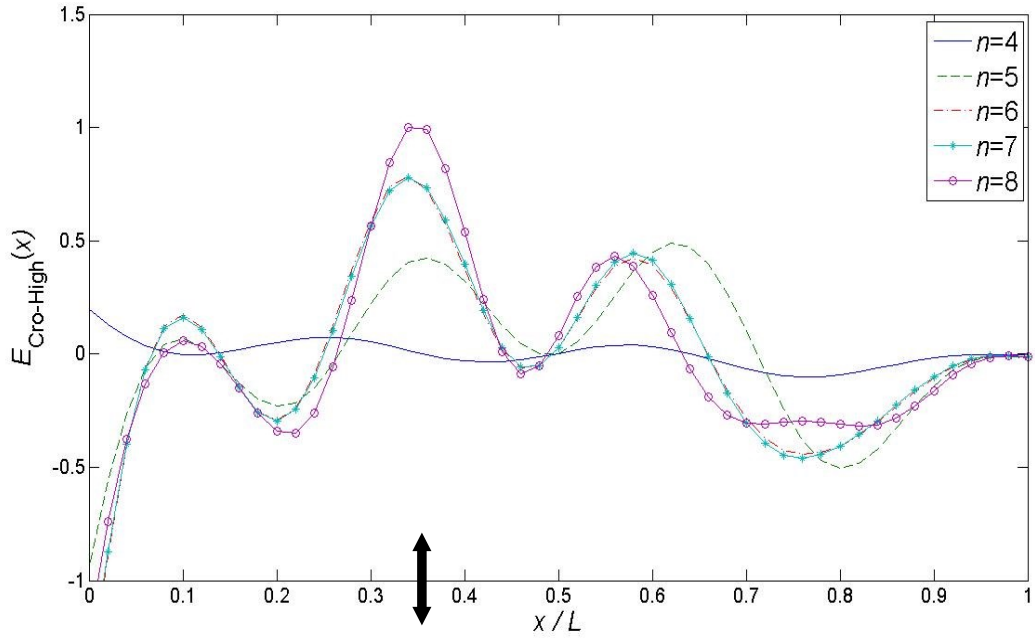
* This figure is normalized through division by the maximum value.

Figure 3.4 FLI under different locations of exciting force (pin-pin boundary condition, $\omega_f = 600\pi$ rad/s, $F_0 = 500$ N, $\alpha = 0$ and $n = 7$)

The results of numerical solution for FLI under fixed-free boundary condition are shown in Fig. 3.5, Fig. 3.6 and Fig. 3.7.

(a) Accumulation phenomenon in FLI

The external exciting force was applied at $x_f = 0.35L$ with driving frequency $\omega_f = 300\pi$ rad/s. The parameter α in Eq. (2.29) was 1, and n was increased from 4 to 8.



* This figure is normalized through division by the maximum value.

Figure 3.5 Accumulation phenomenon in FLI (fixed-free boundary condition, $x_f = 0.35L$, $\omega_f = 300\pi$ rad/s, $F_0 = 500$ N and $\alpha = 1$)

(b) FLI under different driving frequencies of exciting force

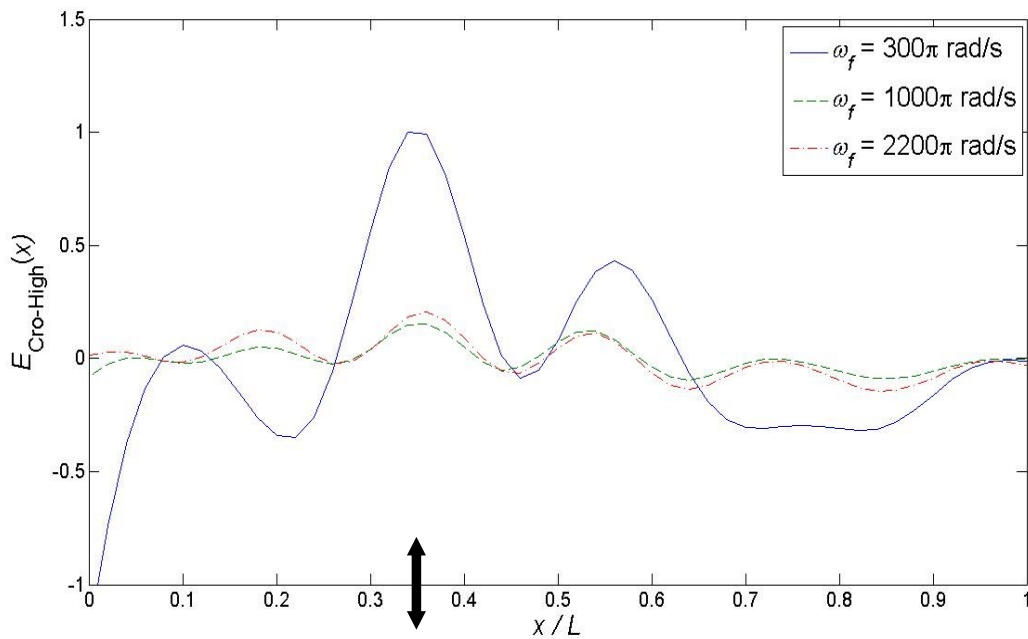
The exciting force was applied at $x_f = 0.35L$ and $\alpha = 1$, $n = 8$. The natural frequencies are shown in Table 3.2. The FLI under different driving frequencies of exciting force are shown in Fig. 3.6.

(c) FLI under different locations of exciting force

The driving frequency of external exciting force is $\omega_f = 300\pi$ rad/s and $\alpha = 1$, $n = 8$. The location of external exciting force varied along the beam. The FLI under different locations of exciting force are shown in Fig. 3.7.

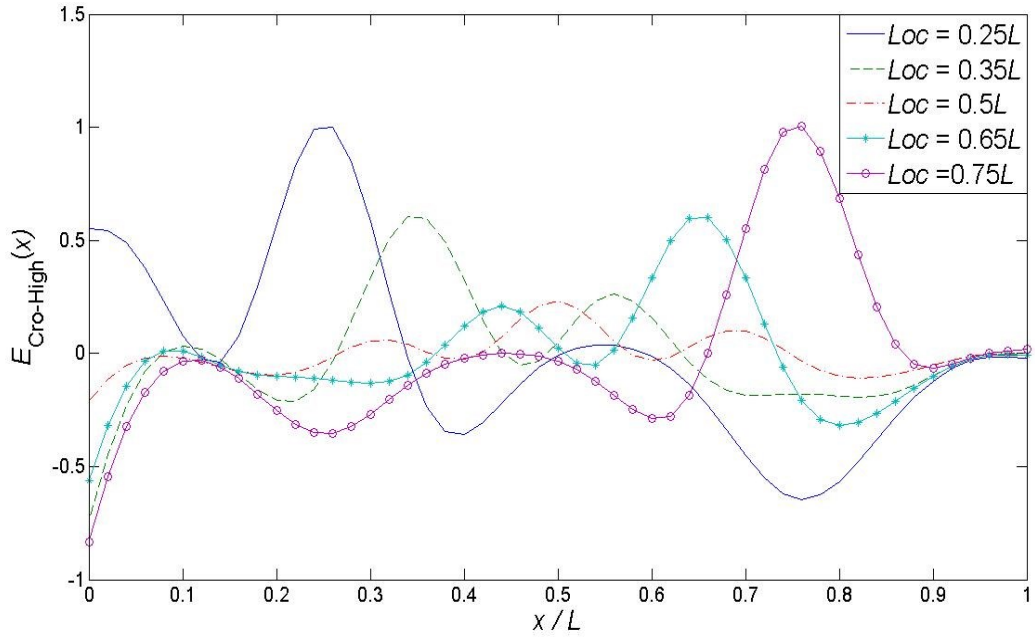
Table 3.2 Natural frequencies obtained in numerical solution (fixed-free boundary condition)

	1 st	2 nd	3 rd	4 th
Natural frequency (rad/s)	87π	543π	1520π	2978π
	5 th	6 th	7 th	8 th
	4924π	7355π	10272π	13676π



* This figure is normalized through division by the maximum value.

Figure 3.6 FLI under different driving frequencies of exciting force (fixed-free boundary condition, $x_f = 0.35L$, $F_0 = 500$ N, $\alpha = 1$ and $n = 8$)



* This figure is normalized through division by the maximum value.

Figure 3.7 FLI under different locations of exciting force (fixed-free boundary condition ($\omega_f = 300\pi$ rad/s, $F_0 = 500$ N, $\alpha = 1$ and $n = 8$))

As mentioned in Section 1.3, the objective of numerical solution is to present the accumulation phenomenon predicted and proved in theoretical part.

This accumulation phenomenon was first directly illustrated by Fig. 3.2 and Fig. 3.5. Both figures depict two phenomena: a growth of FLI at the location of external exciting force and a convergence of the peak to the location, when the number of high order terms is increasing.

The first phenomenon verifies the accumulation phenomenon proved in

Section 2.2. The second one, convergence, can be attributed to the shape of cross-modal energy density element. The low order energy density element, which has long wavelength, can only indicate the location with low accuracy. With the increasing of the parameter n in Eq. (2.29), more high order elements, which can indicate more accurate location, are added into the FLI, and this result in the phenomenon that the next peak after adding is closer to the location. This convergence can give a reasonable prediction of adding higher order element, which is helpful when the high order data are not satisfactory.

The next step is to examine whether this accumulation phenomenon is still valid when the driving frequency and location are different. In Fig. 3.3 and Fig. 3.6, the beam was excited by the force with different driving frequencies. Apart from the decreasing magnitude, which is caused by the decreasing number of cross-modal energy density elements contained in FLI, the location identified by the FLI varies little. This verifies the prediction of Eq. (2.28), which is not affected by the change of driving frequency.

Fig. 3.4 and Fig. 3.7 depict the situation when the location of exciting force is changing. It can found that in Fig. 3.4 at some locations the FLI cannot indicate the location exactly, while in Fig. 3.7 the FLI works well at all

locations. The reason for this may be attributed to the low order cross-modal energy density elements that reduce the accuracy. In Fig. 3.4, the element E_{23} was included in the FLI ($\alpha = 0$ in Eq. (2.29)), while in Fig. 3.7, the lowest order element was E_{34} ($\alpha = 1$ in Eq. (2.29)). As described previously, the long wavelength of low order element may fail to give the prediction with high resolution.

3.3 Summary

This chapter calculated the numerical solution for the illustration of theoretical prediction made in Chapter 2. In Section 3.1, the procedure of energy decomposition and derivation of FLI were shown. It could be found that the decomposition may gradually extract the location information of exciting force. The numerical solution also showed that there is a peak at the location of force in the FLI. In Section 3.2, the numerical solution was calculated to illustrate the accumulation phenomenon of the summation of high order cross-modal energy terms in FLI at the location of exciting force. The simulation also showed that the FLI could localize the force with different driving frequencies and locations.

Chapter 4 Experiment of Cross-Modal Energy Method

In this chapter, the inverse problem in application under experimental condition is presented first. The results of numerical experiment and experimental test are shown to discuss the influence of noise to cross-modal energy method and the verification of this method.

4.1 Inverse problem in experiment

The theory of cross-modal energy was derived in Chapter 2, and the numerical solution was conducted in Chapter 3. However, there is an inverse problem when this theory is applied under experimental condition as a force localization method.

There are two major issues in the inverse problem. The first one is that the calculation of FLI in experiment is different from that in theoretical analysis. Since the location of external exciting force is unknown, the amplification coefficient in Eq. (2.15) cannot be determined through theoretical way. The second one, which often hinders the application of other methods, is the noise. The information to extract amplification coefficients in experiment can just be obtained through measurement, and therefore, the noise is inevitable.

In order to extract the amplification coefficient only through measured mode shapes and operational response with more accuracy under the

influence of noise, the LSM was applied to obtain the FLI in experiment. This is because according to Eq. (2.5) the extraction of amplification coefficient is a typical inverse problem (See Appendix A). According to the references [2, 8, 17, 21, 32] in Section 1.1, LSM and its advanced application can effectively improve the ill-condition, and thus the influence of noise.

After determining procedure of calculating the FLI under experiment condition, it is important to analyze the influence of noise on this method. According to the LSM and definition of the FLI, the noise can influence the FLI in two ways: affecting the extraction of amplification coefficient and derivative of mode shapes. The details can be found in Fig. 4.13.

Numerical experiment was conducted to simulate the experiment test and investigate the influence of noise on FLI. Following the numerical experiment, an experimental test was performed to verify the method under experimental condition.

In numerical experiment, in order to analyze the noise resistance of the proposed method, two different levels of random noise, 3% and 30%, were added to the theoretically calculated mode shapes and operational response of forced vibration displacement. To investigate the effects of amplification of noise due to the derivative of mode shapes during the procedure, a noise

reduction method was applied to reduce only the amplification of noise caused by derivative.

4.2 Numerical experiment

In this section, the results of numerical experiment for different boundary conditions, different noise levels and different noise reduction methods are shown to analyze the influence of noise on the proposed method.

The beam model examined in the numerical experiment is the same as that in the numerical solution. The results in numerical experiment can make a comparison with those in numerical solution. And, the numerical experiment may also give a reasonable prediction of experimental test. The random noise in operational displacement response and mode shapes was added by *Matlab* command *rand*. In order to simulate the experimental condition and obtain better results, before applying LSM, the noised data was averaged by 500 times. The reason for averaging 500 times is to simulate the magnitude average function in laser vibrometer used in the experimental test.

The results of numerical experiment under pin-pin and fixed-free boundary conditions are shown respectively by the following figures.

(a) 3% random noise under pin-pin boundary condition

The external exciting force was applied at $x_f = 0.35L$ with driving frequency $\omega_f = 600\pi$ rad/s between 1st and 2nd modes, when the beam was in pin-pin boundary condition. The parameter α in Eq. (2.29) was 0, and n was increased from 3 to 7. The magnitude of external exciting force F_0 was 500 N in all the cases of numerical experiment. The interval between two measured points was $0.01L$. The displacement response and mode shapes of the beam with 3% random noise are shown by Fig. 4.1 and Fig. 4.2, where the mode shapes are mass-normalized.

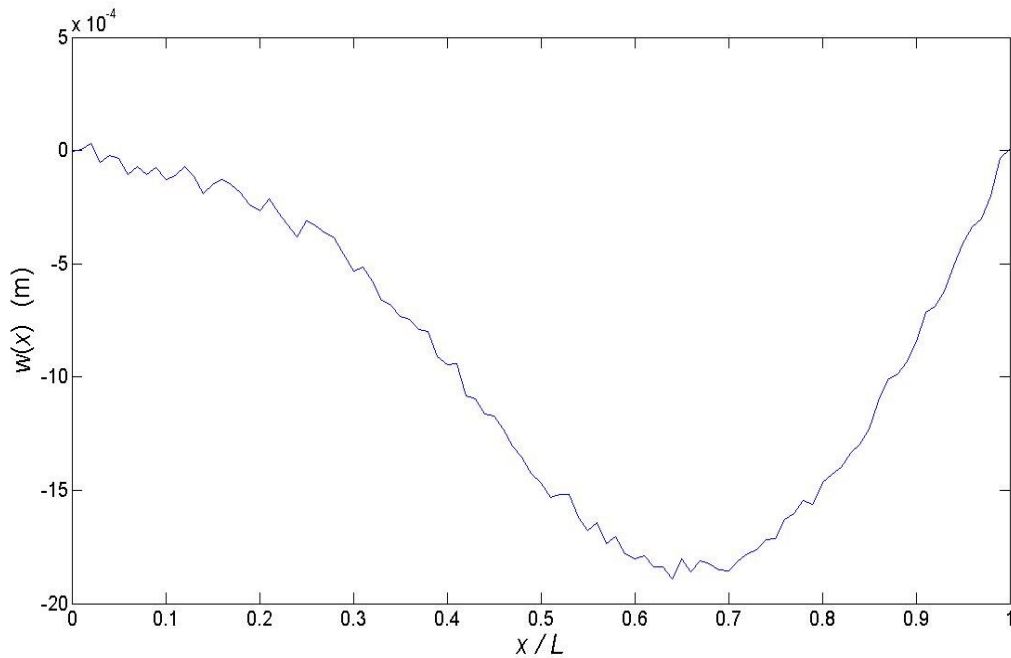


Figure 4.1 Displacement response with 3% random noise (pin-pin boundary condition)

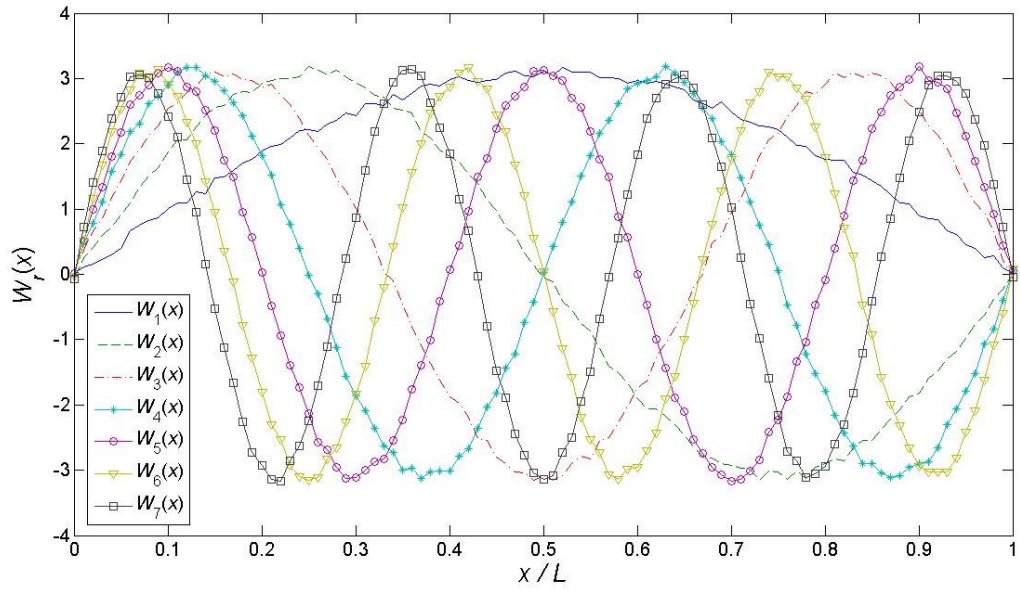


Figure 4.2 Mode shapes with 3% random noise (pin-pin boundary condition)

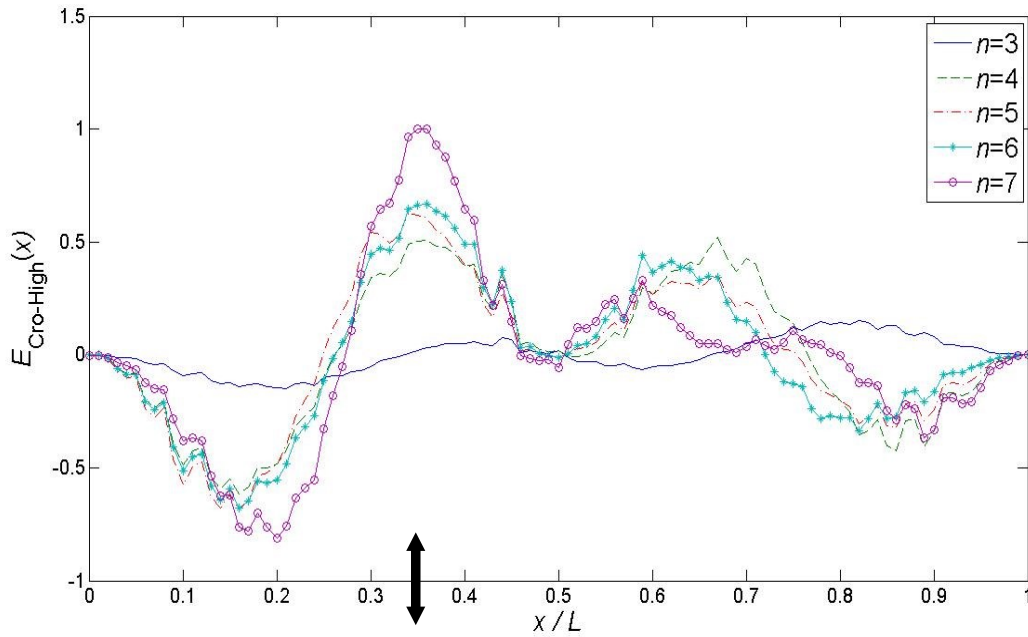
On the basis of displacement response and mode shapes, the modal ratio coefficient η_r was extracted through LSM as illustrated in Appendix A.

All the modal ratio coefficients in different modes are listed in Table 4.1 with the theoretical values which was calculated through Eq. (2.6).

Table 4.1 Extracted and theoretical modal ratio coefficients (pin-pin boundary condition)

Order	η_r (Extracted)	η_r (Theoretical)	Error (%)
1	-4.6470e-4	-4.6535e-4	0.14
2	2.1669e-4	2.1586e-4	0.38
3	-5.5432e-6	-6.7273e-6	17.60
4	-1.0102e-5	-1.0948e-5	7.73
5	-3.0327e-6	-4.0122e-6	24.41
6	6.3591e-7	1.6077e-7	295.54
7	1.0947e-6	7.3594e-7	48.75

By substituting the calculated modal ratio coefficients into Eq. (2.29), the FLI was obtained. The calculated FLIs with varying n are shown in Fig. 4.3.



* This figure is normalized through division by the maximum value.

Figure 4.3 FLI calculated in numerical experiment (pin-pin boundary condition, $x_f = 0.35L$, $\omega_f = 600\pi$ rad/s, $F_0 = 500$ N and $\alpha = 0$)

(b) 3% random noise under fixed-free boundary condition

In this case, the same beam model was under fixed-free boundary condition. The external exciting force was applied at $x_f = 0.35L$ with driving frequency $\omega_f = 300\pi$ rad/s. The parameter α in Eq. (2.29) was 1, and n was increased from 4 to 8. The interval between two measured points was $0.01L$.

As the same procedure in case (a), the displacement response with 3% random noise is shown by Fig. 4.4. The mass-normalized mode shapes with 3% random noise are shown in Fig. 4.5. All the extracted modal ratio coefficients in different modes are listed in Table 4.2 with the theoretical values. The calculated FLIs with varying n are shown in Fig. 4.6.

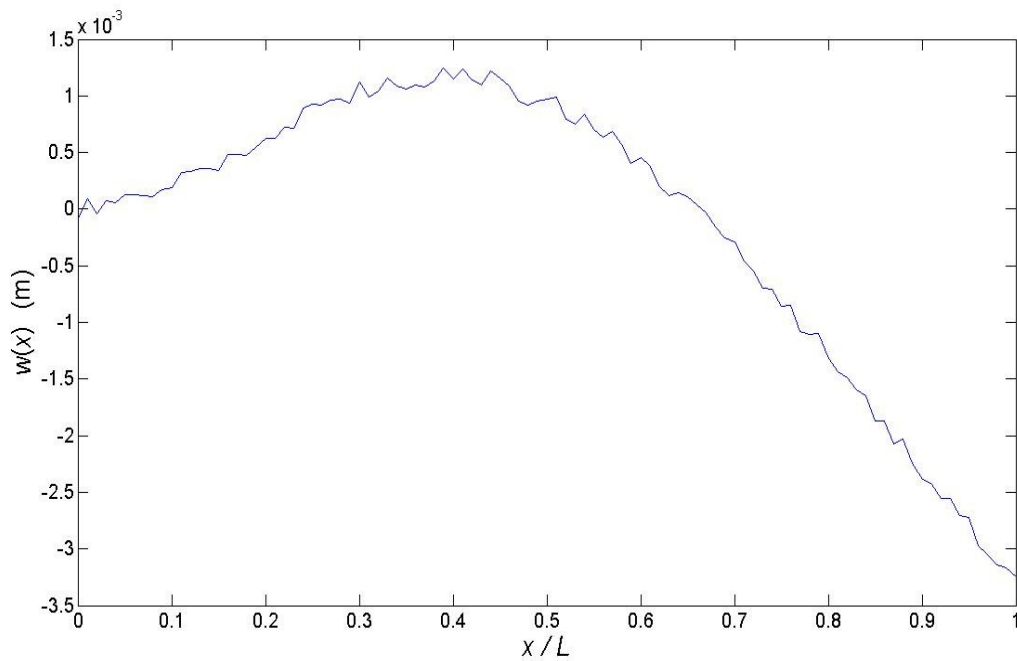


Figure 4.4 Displacement response with 3% random noise (fixed-free boundary condition)

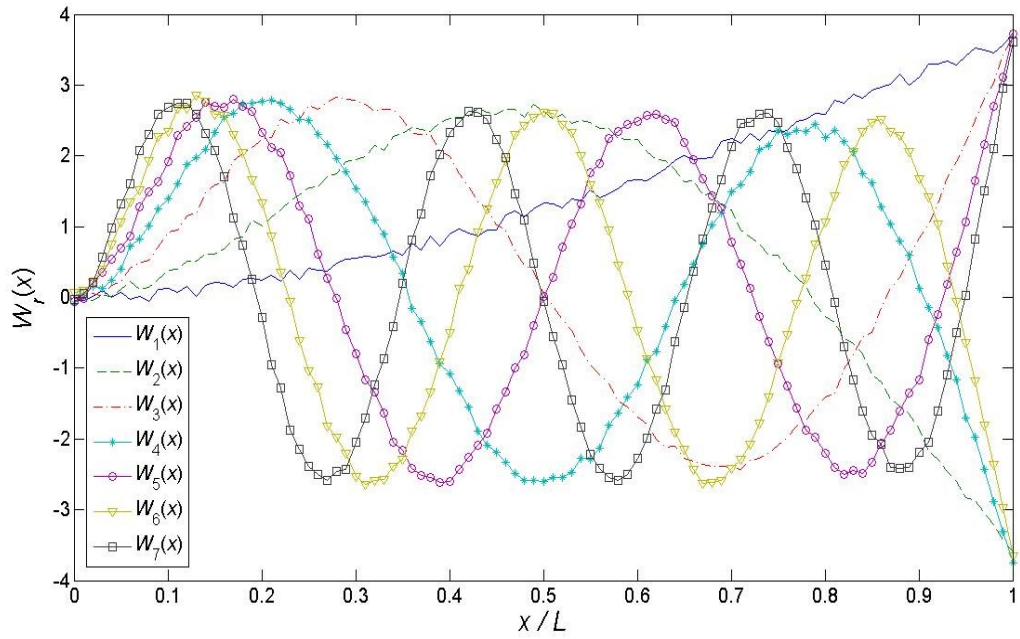
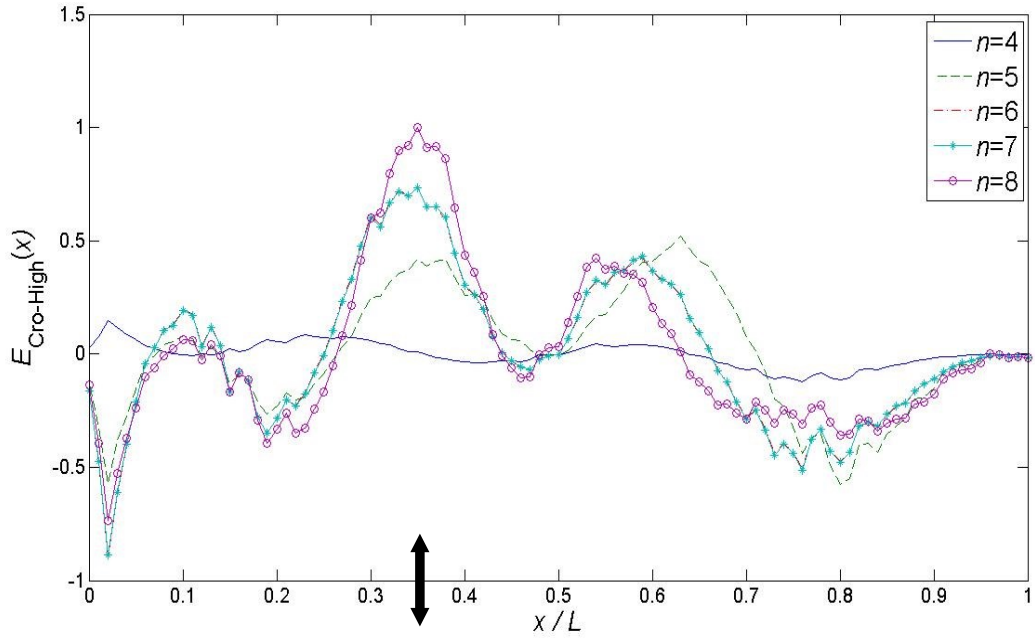


Figure 4.5 Mode shapes with 3% random noise (fixed-free boundary condition)

Table 4.2 Extracted and theoretical modal ratio coefficients (fixed-free boundary condition)

Order	η_r (Extracted)	η_r (Theoretical)	Error (%)
1	-4.0559e-4	-4.0558e-4	0.002
2	5.5826e-4	5.5829e-4	0.005
3	5.7239e-5	5.7330e-5	0.16
4	1.4635e-6	1.3849e-6	5.68
5	-4.7274e-6	-4.5902e-6	2.99
6	-2.0825e-6	-2.0611e-6	1.04
7	1.5506e-7	9.8671e-8	57.15
8	6.6776e-7	6.4651e-7	3.29



* This figure is normalized through division by the maximum value.

Figure 4.6 FLI calculated in numerical experiment (fixed-free boundary condition, $x_f = 0.35L$, $\omega_f = 300\pi$ rad/s, $F_0 = 500$ N and $\alpha = 1$)

(c) 30% random noise under pin-pin and fixed-free boundary conditions

In order to examine the noise resistance of cross-modal energy method and simulate the operational condition where the random noise is significantly high, 30% random noise were added into the theoretical displacement response, while the mode shapes were still at 3% level. Before applying LSM, the noised data for both displacement response and mode shapes was averaged by 500 times. The displacement response under pin-pin boundary condition with 30% random noise and the corresponding FLI were simulated and are shown in Fig. 4.7 and Fig. 4.8. The interval between two

measured points was $0.01L$.

For the fixed-free boundary condition, the displacement response with 30% random noise and the corresponding FLI were simulated and are shown in Fig. 4.9 and Fig. 4.10. The interval between two measured points was $0.01L$.

(d) Reduction in noise caused by high order derivative

By reasonably increasing the interval between measured points applied in the simulation, the noise amplified by high order derivative, which is calculated through finite-difference method, can be considerably reduced with acceptable filtering of information in the original function [38]. In this case, interval between two measured points was changed from $0.01L$ to $0.02L$ during the calculation of derivative, while the modal ratio coefficients were still calculated under the interval of $0.01L$. The FLIs calculated with 30% random noise after applying this noise reduction method are shown in Fig. 4.11 and Fig. 4.12.

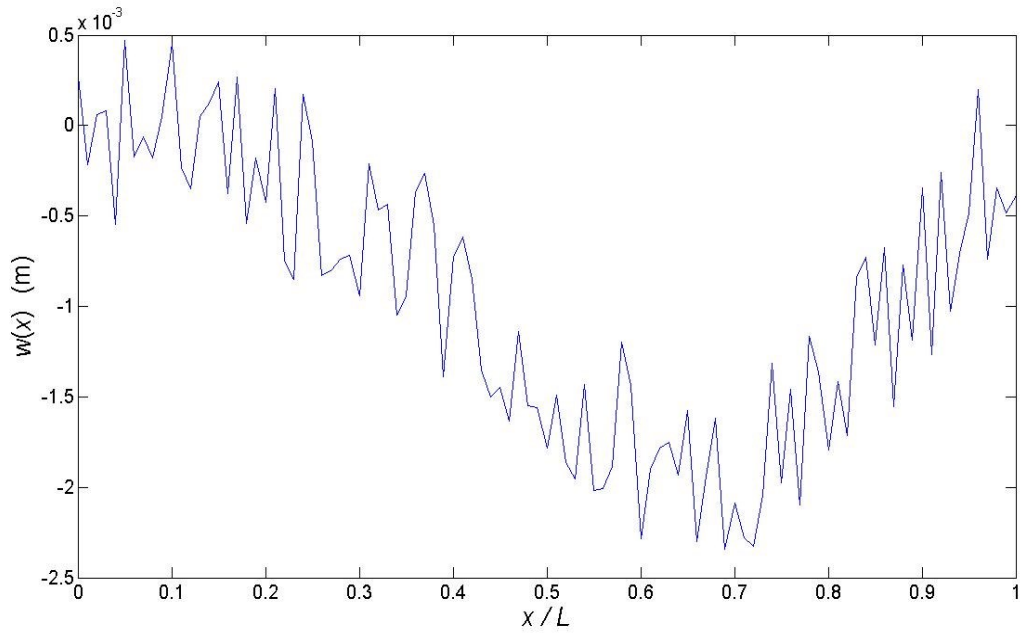
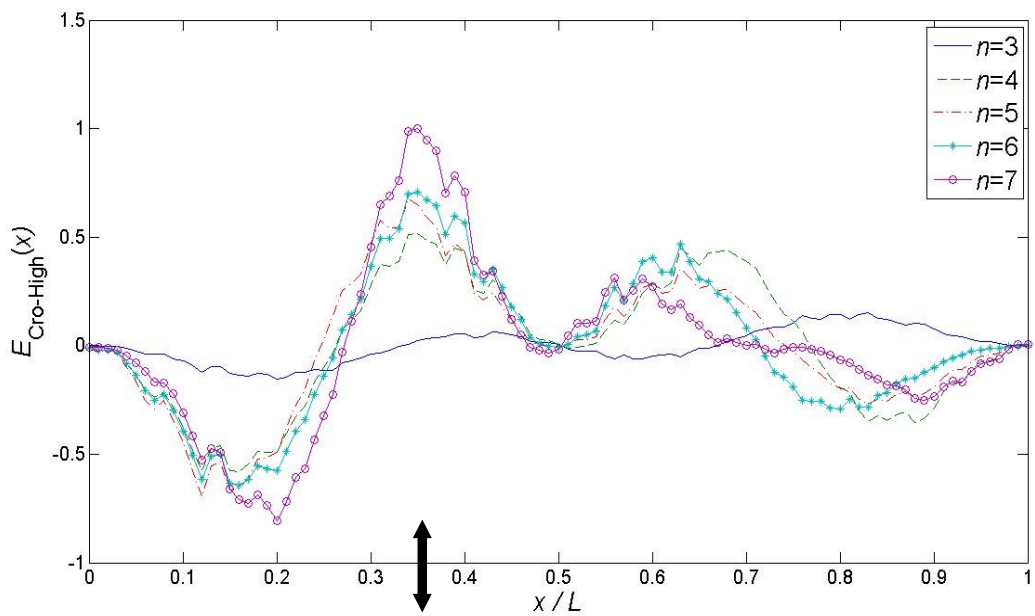


Figure 4.7 Displacement response with 30% random noise (pin-pin boundary condition)



* This figure is normalized through division by the maximum value.

Figure 4.8 FLI calculated with 30% random noise (pin-pin boundary condition, $x_f = 0.35L$, $\omega_f = 600\pi$ rad/s, $F_0 = 500$ N and $\alpha = 0$)

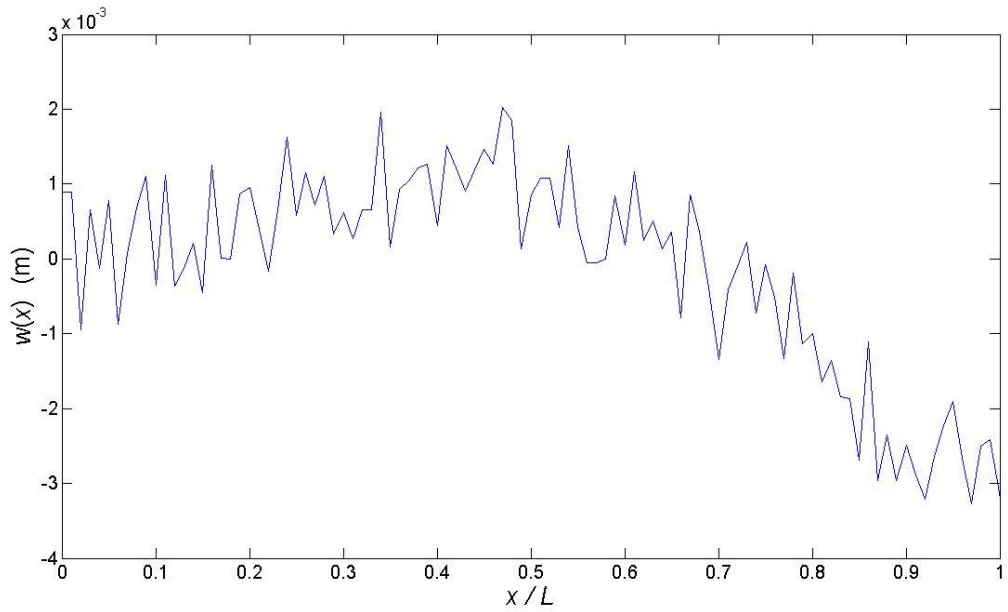
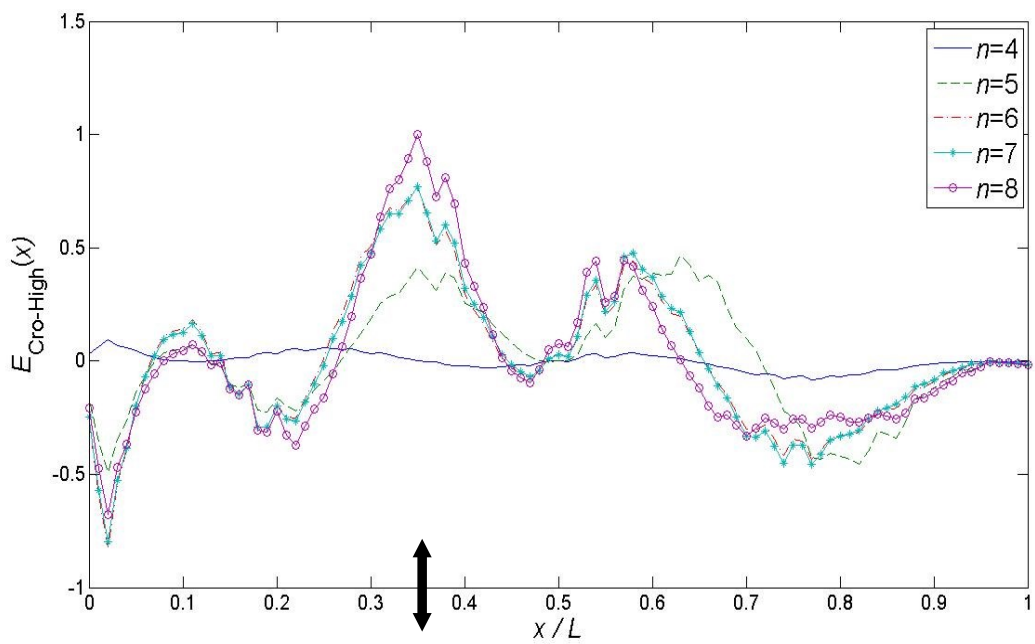
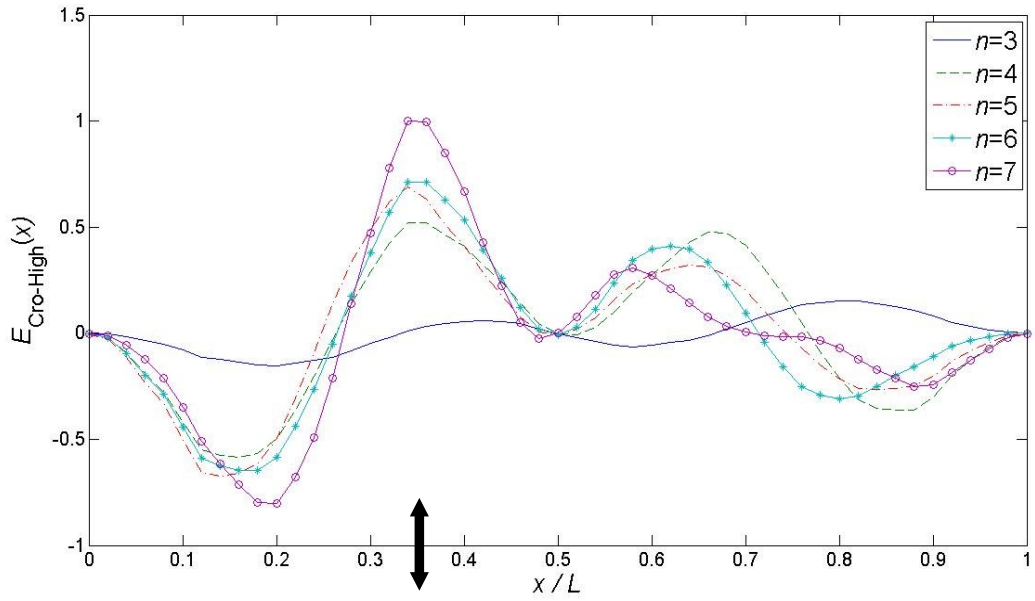


Figure 4.9 Displacement response with 30% random noise (fixed-free boundary condition)



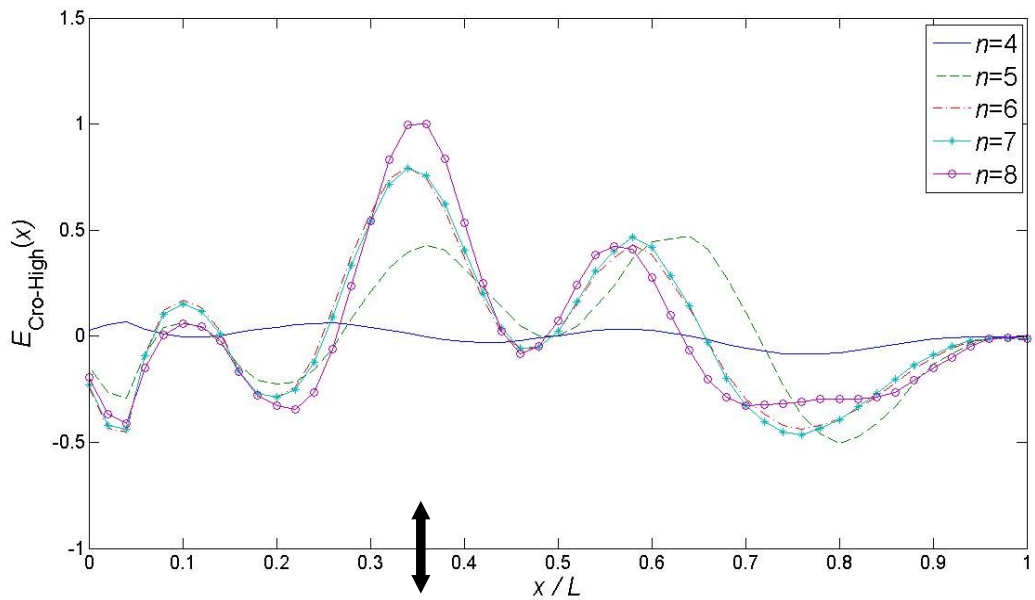
* This figure is normalized through division by the maximum value.

Figure 4.10 FLI calculated with 30% random noise (fixed-free boundary condition, $x_f = 0.35L$, $\omega_f = 300 \pi$ rad/s, $F_0 = 500$ N and $\alpha = 1$)



* This figure is normalized through division by the maximum value.

Figure 4.11 FLI calculated with 30% random noise after reducing the noise amplified by derivative (pin-pin boundary condition, $x_f = 0.35L$, $\omega_f = 600\pi$ rad/s, $F_0 = 500$ N and $\alpha = 0$)



* This figure is normalized through division by the maximum value.

Figure 4.12 FLI calculated with 30% random noise after reducing the noise amplified by derivative (pin-pin boundary condition, $x_f = 0.35L$, $\omega_f = 300\pi$ rad/s, $F_0 = 500$ N and $\alpha = 0$)

The numerical experiment aims to investigate the influence of noise on cross-modal energy method. As shown in Fig. 4.13, the noise can contaminate the result in two different ways during the procedure of cross-modal energy method: (1) modal ratio coefficient and (2) cross-modal energy density element.

Tables 4.1 and 4.2 show the influence of noise on the extraction of modal ratio coefficient. The 3% noise in mode shapes and operational response, although averaged by 500 times, still caused some errors in the extracted modal ratio coefficients. The error is related to the value of modal ratio coefficient. The larger value may suffer less error, while the smaller one can contain more error. By comparing the calculated FLI in numerical experiment (Fig. 4.3 and Fig. 4.6) with the theoretical one in numerical solution (Fig. 3.2 and Fig. 3.5), it can be found that although some considerably large errors were in the coefficients (like 295.54% in Table 4.1) little deviation from the exact location of force was caused. This suggests that the cross-modal energy method is not very sensitive to the noise in the extracted modal ratio coefficient.

Another part of the FLI suffering from noise is the cross-modal energy density element, where the noise is amplified by the high order differentiation process. This effect can be found through the serious

fluctuation in Fig. 4.3 and Fig. 4.6.

It has to be emphasized that the modal ratio coefficient and cross-modal energy density element have different importance in FLI. As shown in Eq. (2.6), the important information about the location of external exciting force is contained in modal ratio coefficient. This suggests that: (1) the noise in modal ratio coefficient should be reduced carefully (in case of losing the useful information), but is not serious; (2) the noise in cross-modal energy density element is serious (since amplified by high order derivative), but has limited effect on the accuracy of FLI.

These suggestions provide a certain advantage of the proposed method over the FAT method, which directly based on the fourth order derivative of response. Since the noise amplified by high order derivative do not contain location information and can be filtered separately in cross-modal energy method, the well-designed filter used in FAT can be avoided in the new method.

In order to investigate the ability to cope with high level noise 30% noise (instead of 3%) was assumed in the operational response, as shown in Fig. 4.8 and Fig. 4.10. After averaging, the FLI shows slight difference from that for 3% noise. This implies that the problem caused by random noise can be handled by enough averaging.

In another experiment, a noise reduction method was applied in order to moderate the noise amplified by high order derivative. Fig. 4.11 and Fig. 4.12 show the improved FLI. It can be found that the noise in cross-modal energy density elements is considerably smoothed with slight change of the indicated location. This proves that the amplified noise in cross-modal energy density element has limited effects on localizing the force and can be filtered out thoroughly without obvious harm to FLI.

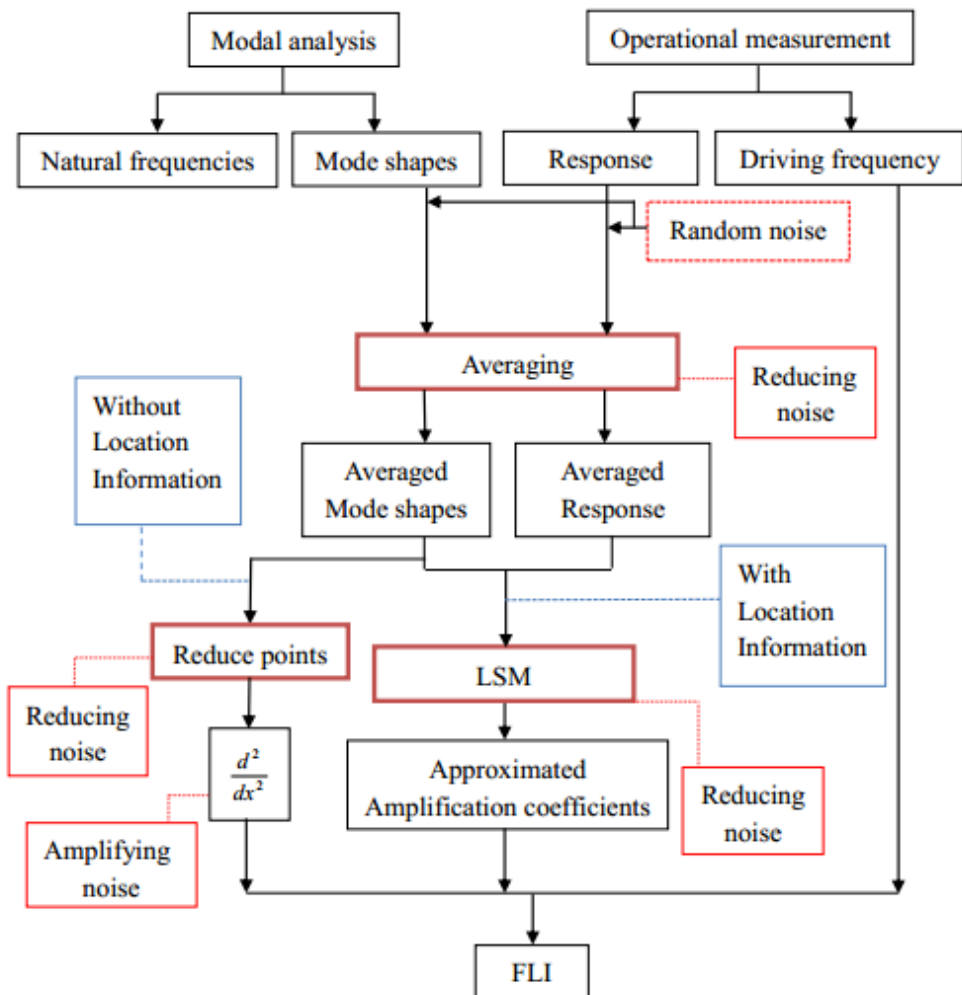


Figure 4.13 Influence of noise on cross-modal energy method

4.3 Experimental test of the cross-modal energy method

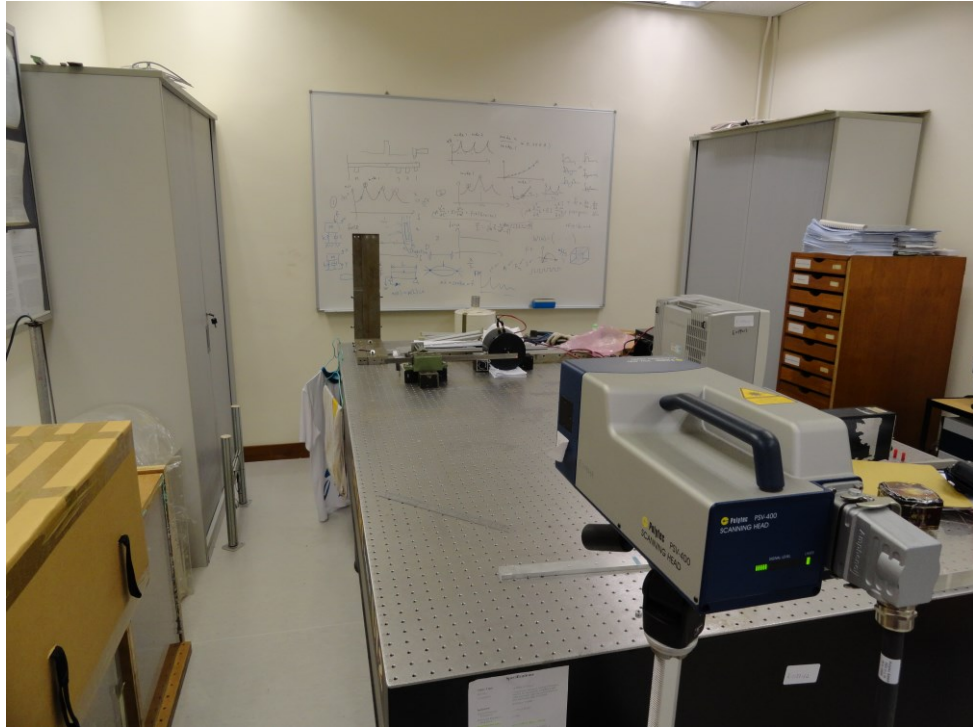
In this section, the experimental set-up, procedure and results are illustrated to verify the cross-modal energy method in determining the location of exciting harmonic force.

4.3.1 Experimental set-up

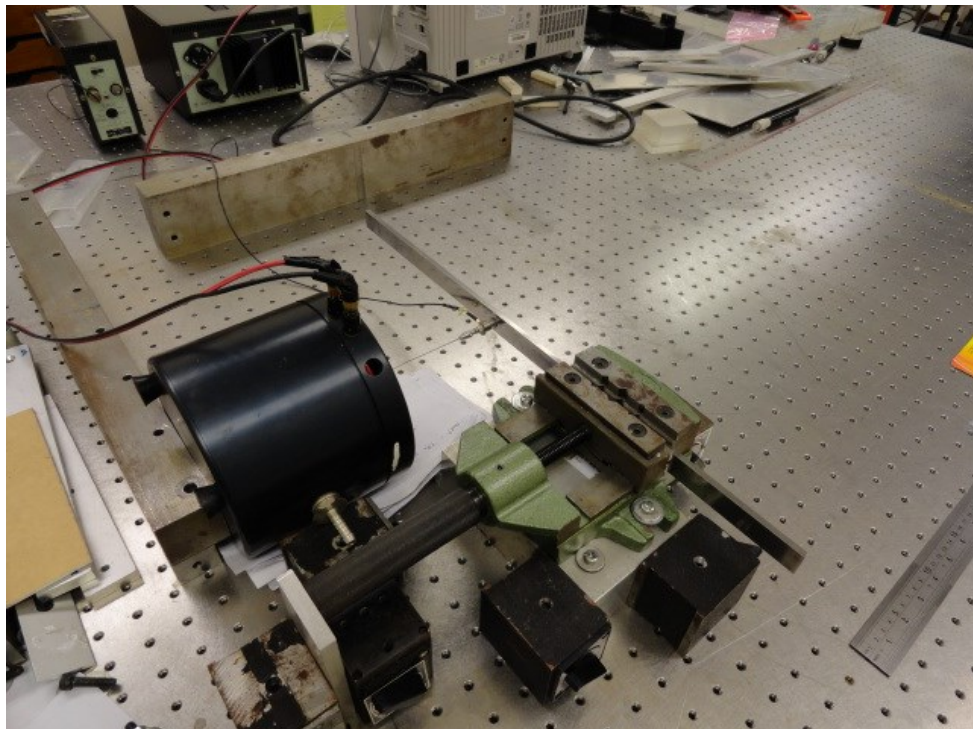
A uniform beam in the fixed-free boundary condition was examined. The beam is made of mild steel with the same geometric parameters described in numerical solution and numerical experiment. The density and Young's modulus of mild steel were assumed to be $\rho = 7740 \text{ kg/m}^3$ and $Y = 204 \text{ GPa}$.

The beam was excited by a concentrated force applied by the shaker (B&K Type 4809) powered by power amplifier (B&K Type 2706). The force transducer (B&K Type 8203) was connected between the beam and shaker with glue. Modal parameters and operational response were measure by using laser vibrometer (Polytec PSV-400). The signal obtained from the force transducer was amplified by the charge amplifier (B&K Type 2635).

Fig. 4.14 shows the experimental set-up.



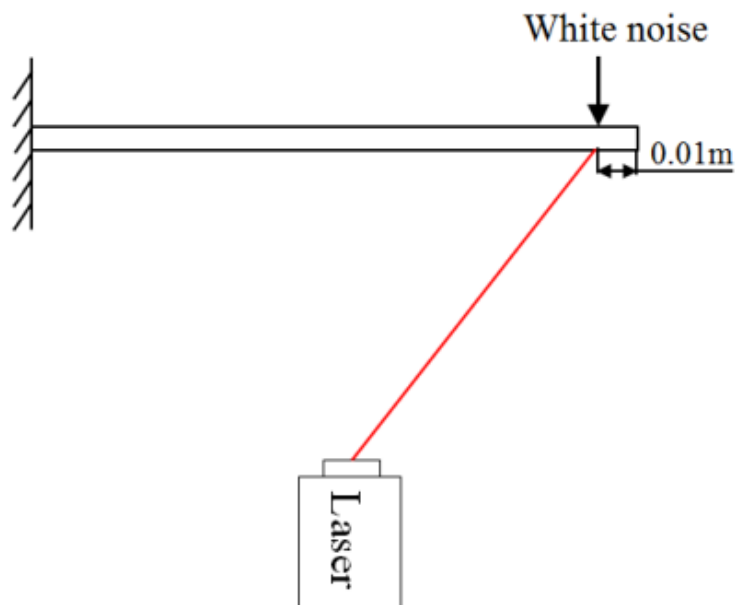
(a) Laser vibrometer



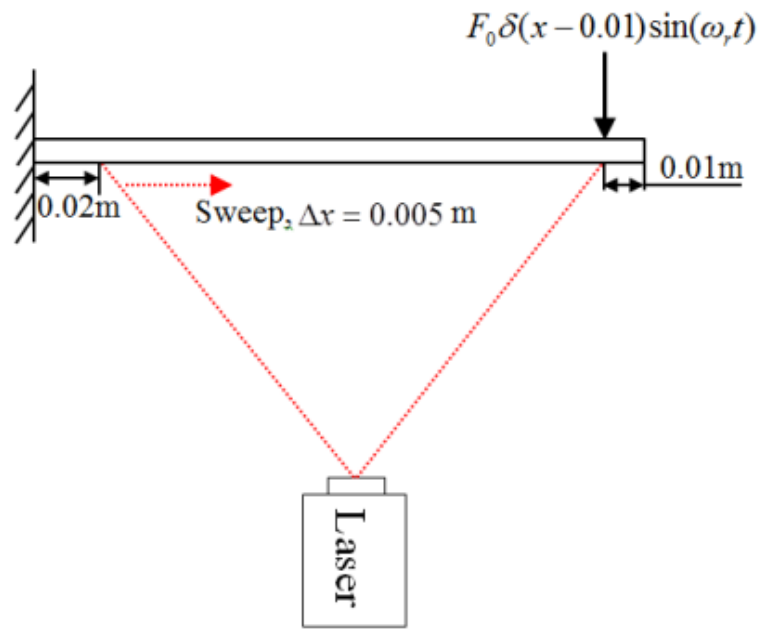
(b) Beam and excitation

Figure 4.14 Set-up of experimental test

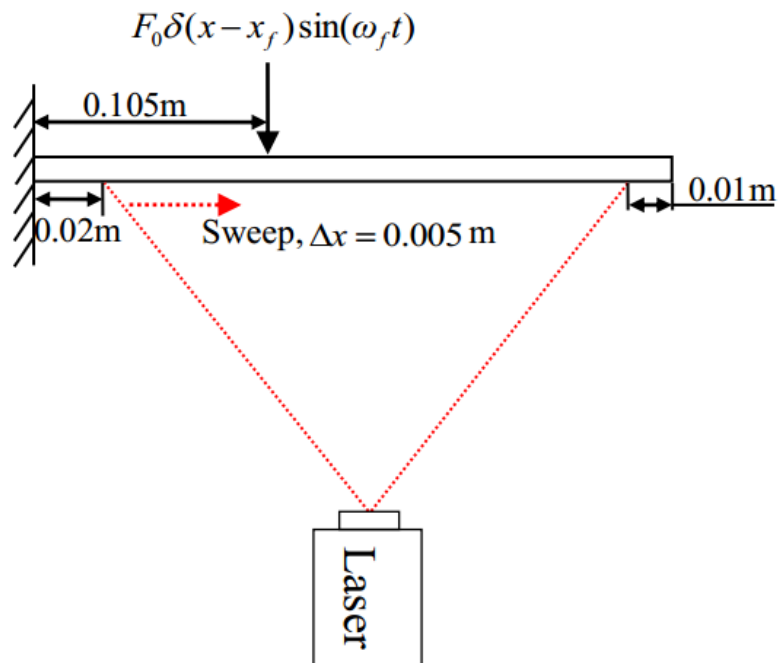
In order to calculate the FLI and find the location of exciting force, both the mode shapes and operational response are required. The mode shapes were measured by exciting the fixed-free beam at the free end with the corresponding natural frequencies. The natural frequencies were obtained from the peaks in point mobility FRF through modal testing. The velocity response was measured under the operational condition, where the beam was excited by the shaker at the location to identify. The measurement procedure is illustrated by Fig. 4.15.



(a) Measurement of point mobility FRF



(b) Measurement of mode shapes



(c) Measurement of operational velocity response

Figure 4.15 Measurement procedures in experimental test

As shown in Fig. 4.15(a), the excitation and measurement points for measuring point mobility FRF were chosen at the location 0.01 m away from the free end. White noise was applied to obtain the result in a broad frequency band. In Fig. 4.15(b), the beam was excited by the external force under the natural frequency ω_r at the same location to get the Operational Detection Shape (ODS) as the corresponding mode shape. The laser vibrometer swept from the point 0.02 m away from the fixed end to the one 0.01 m away from the free end, and the interval between two measured points is 0.005 m. In Fig. 4.15(c), the setting of the sweeping range was the same as that in Fig. 4.15(b), and the external exciting force was applied at the location $x_f = 0.35L$ with the driving frequency $\omega_f = 300\pi$ rad/s, while the magnitude F_0 was not under control. The reason that only 7 mode shapes were measured is that higher mode shapes are with less accuracy and in practice only limited mode shapes are available.

In the experiment, the point mobility FRF was approximated by H_2 with 500-times complex average [6]. The measured mode shapes and operational displacement response were measured with 500-times magnitude averaging.

4.3.2 Results of experiment

The point mobility FRF measured by the procedure illustrated in Fig.

4.15(a) is shown in Fig. 4.16.

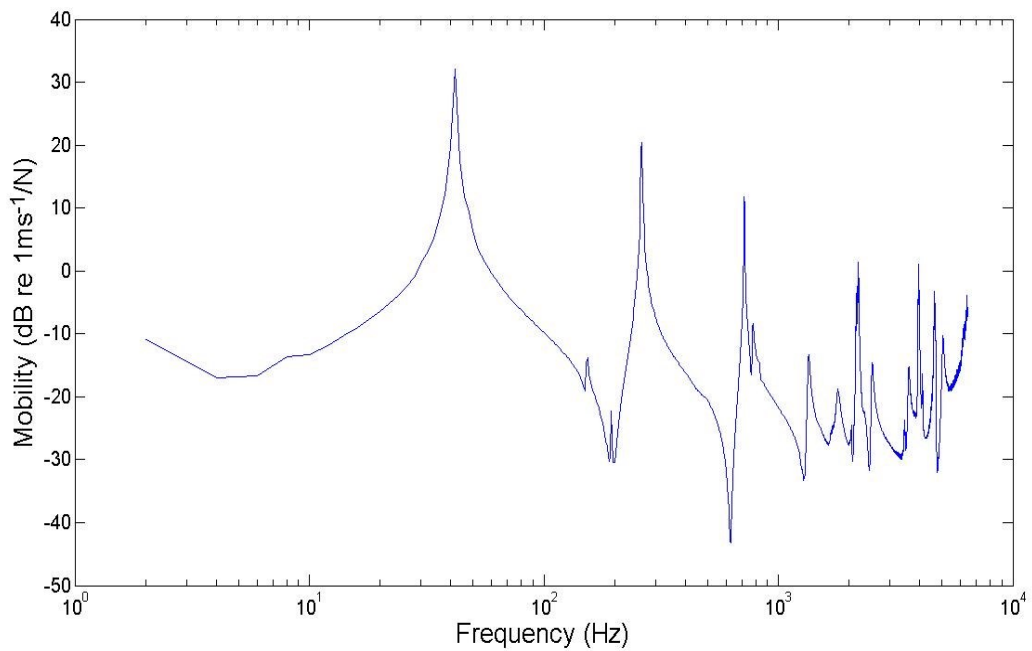


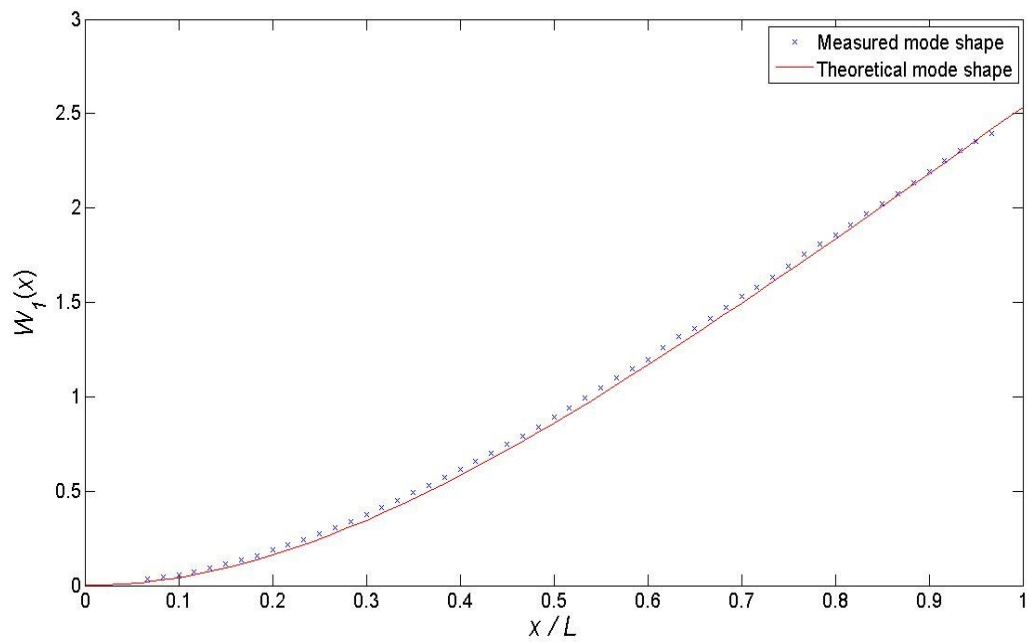
Figure 4.16 Point mobility FRF using white noise

The measured natural frequencies obtained from the peaks in Fig. 4.16 are listed in Table 4.3 as well as the theoretical values simulated in numerical solution. (The values are changed to circular frequencies)

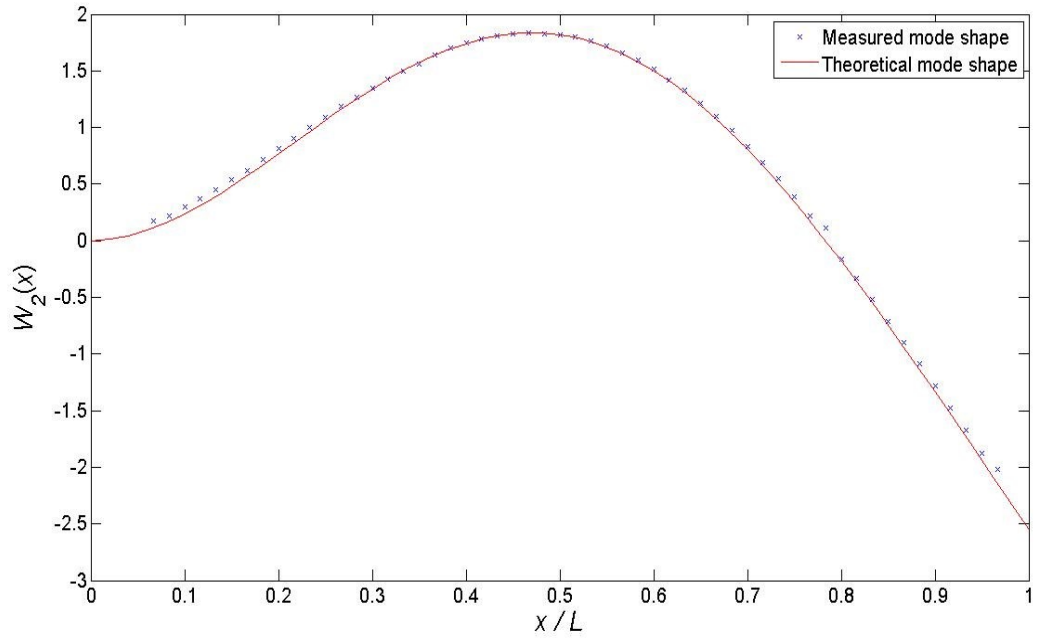
As illustrated in Fig. 4.15(b), the mode shapes were measured by exciting the beam with the corresponding natural frequencies. The measured mass-normalized mode shapes are shown in Fig. 4.17 with the theoretical ones.

Table 4.3 Measured natural frequencies with theoretical values

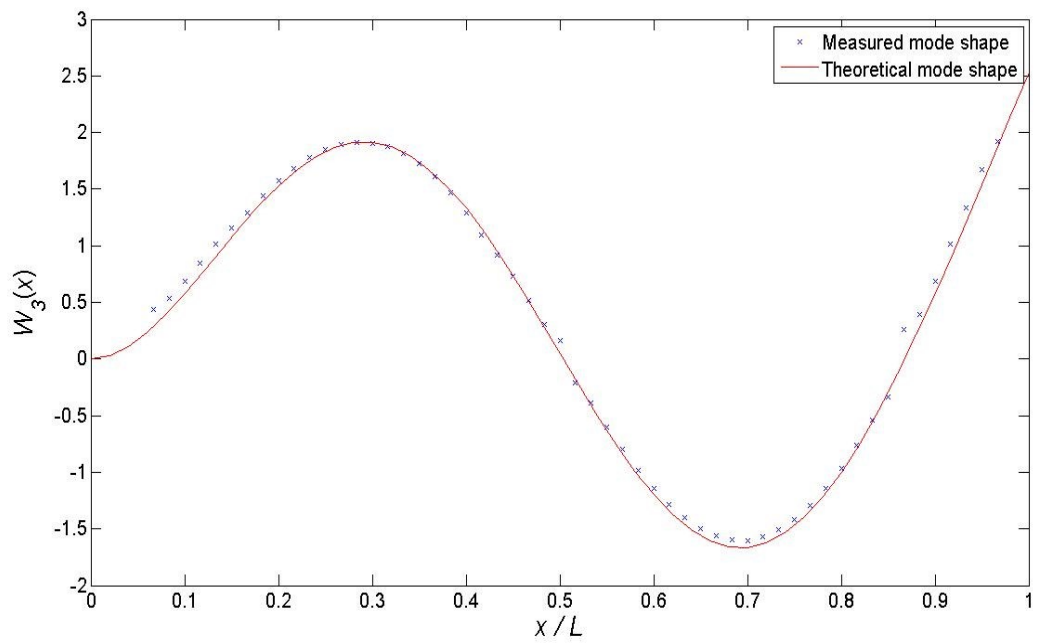
Order	ω_r (Measured, rad/s)	ω_r (Theoretical, rad/s)	Difference (%)
1	88π	87π	1.15
2	524π	543π	3.50
3	1432π	1520π	5.79
4	2700π	2978π	9.33
5	5036π	4924π	2.27
6	8266π	7355π	12.39
7	10060π	10272π	2.06



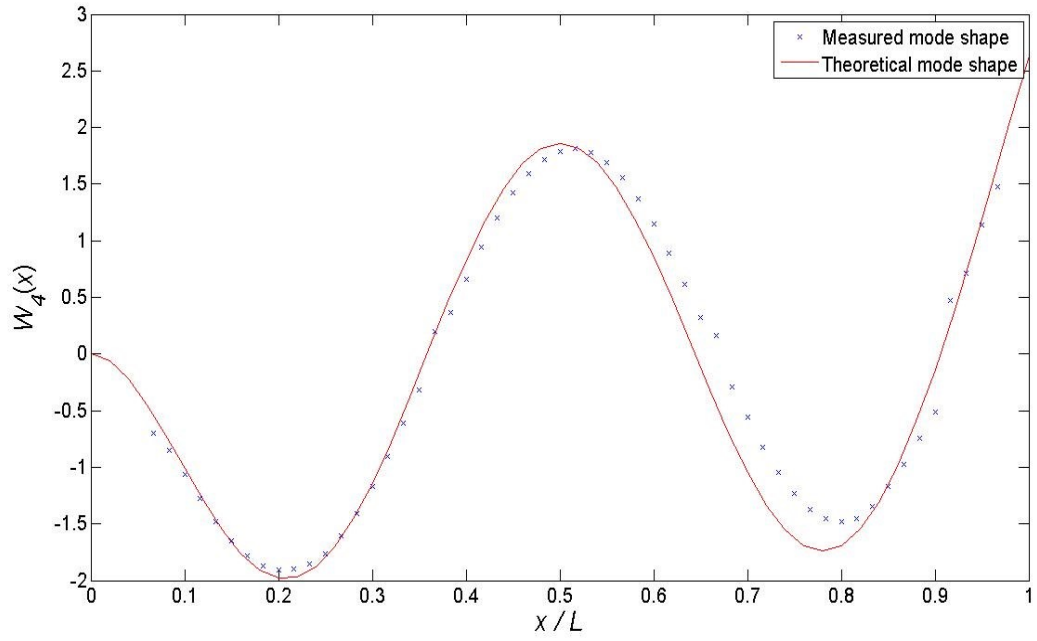
(a) 1st mode shape



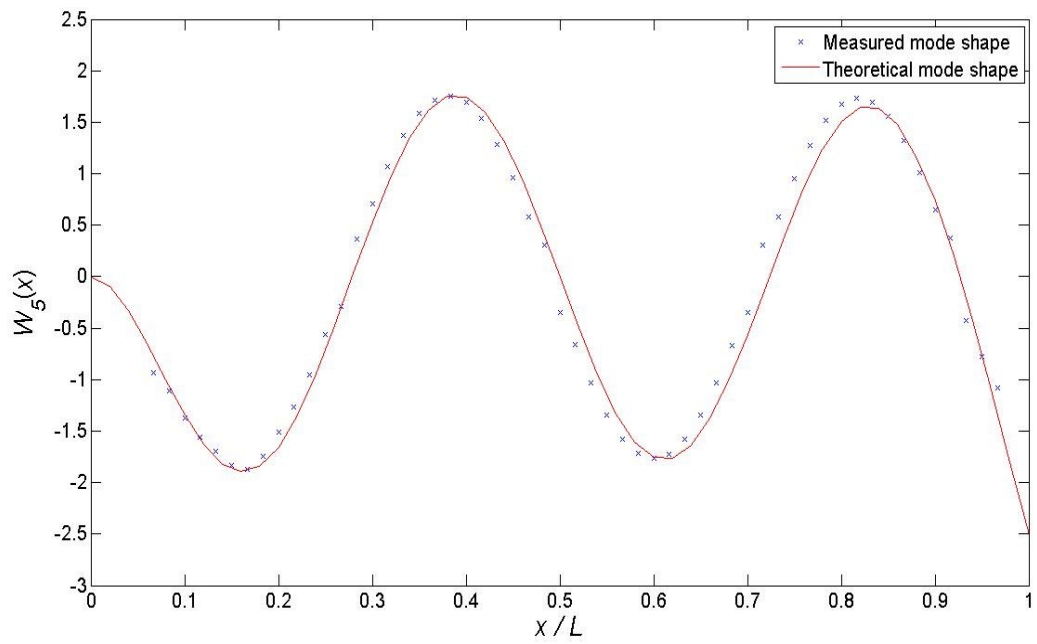
(b) 2nd mode shape



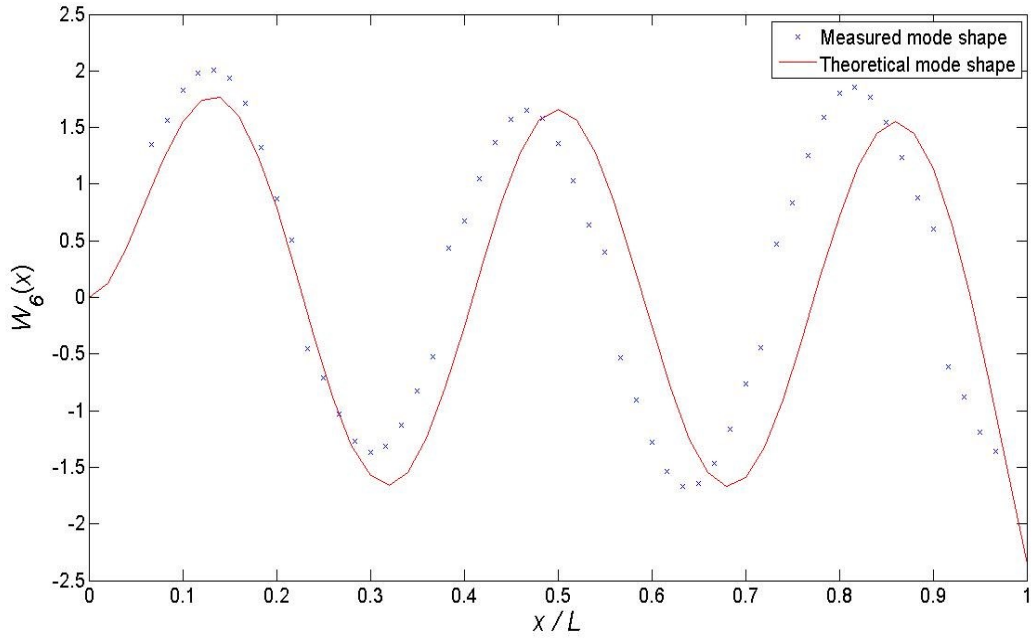
(c) 3rd mode shape



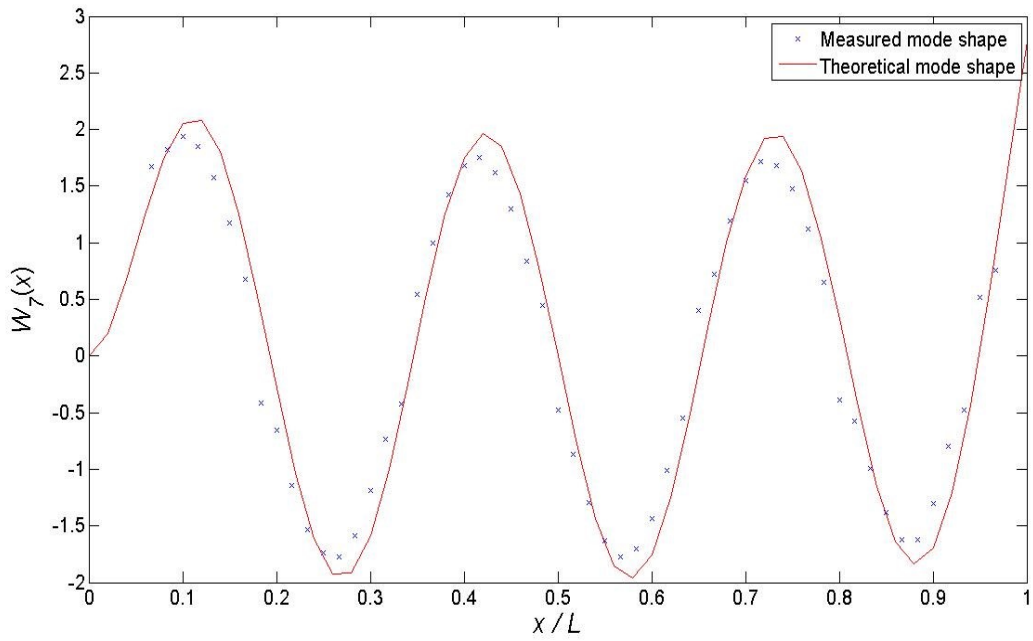
(d) 4th mode shape



(e) 5th mode shape



(f) 6th mode shape



(g) 7th mode shape

Figure 4.17 Mass-normalized measured and theoretical mode shapes

Under the procedure shown in Fig. 4.15(c), the operational velocity was measured and shown in Fig. 4.18.

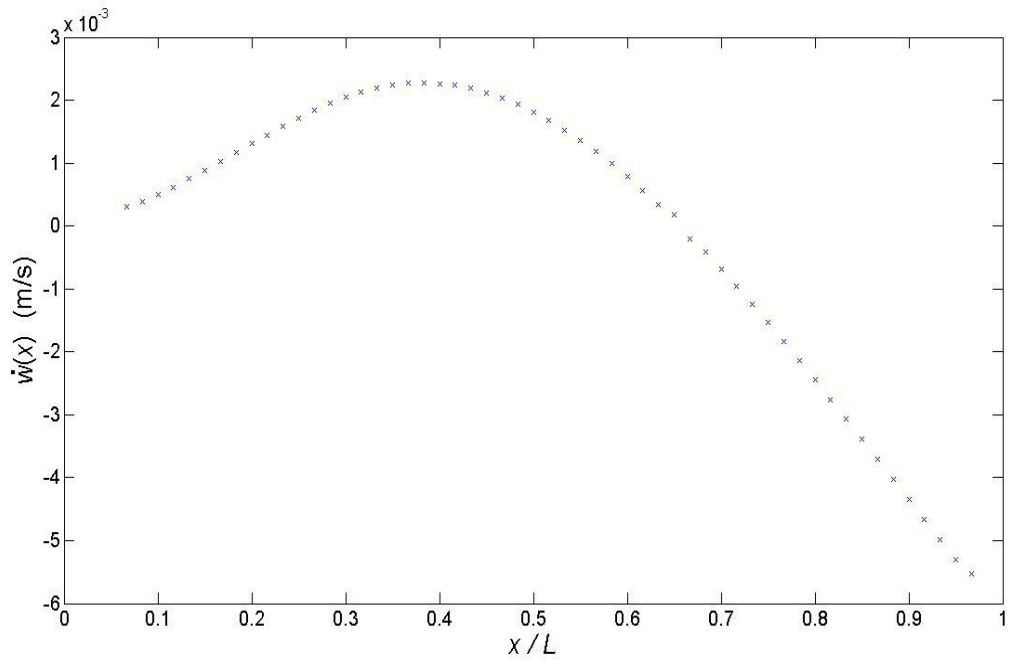


Figure 4.18 Measured operational velocity response

On the basis of the measured mode shapes and operational response, the modal ratio coefficient η_r was extracted through LSM. All the modal ratio coefficients in different modes are listed in Table 4.4.

Table 4.4 Modal ratio coefficients in experimental test

	1 st	2 nd	3 rd	4 th
η_r	-1.1962e-6	1.6566e-6	1.8329e-7	-8.6184e-9
	5 th	6 th	7 th	
	1.5549e-8	-9.0791e-9	-6.0299e-10	

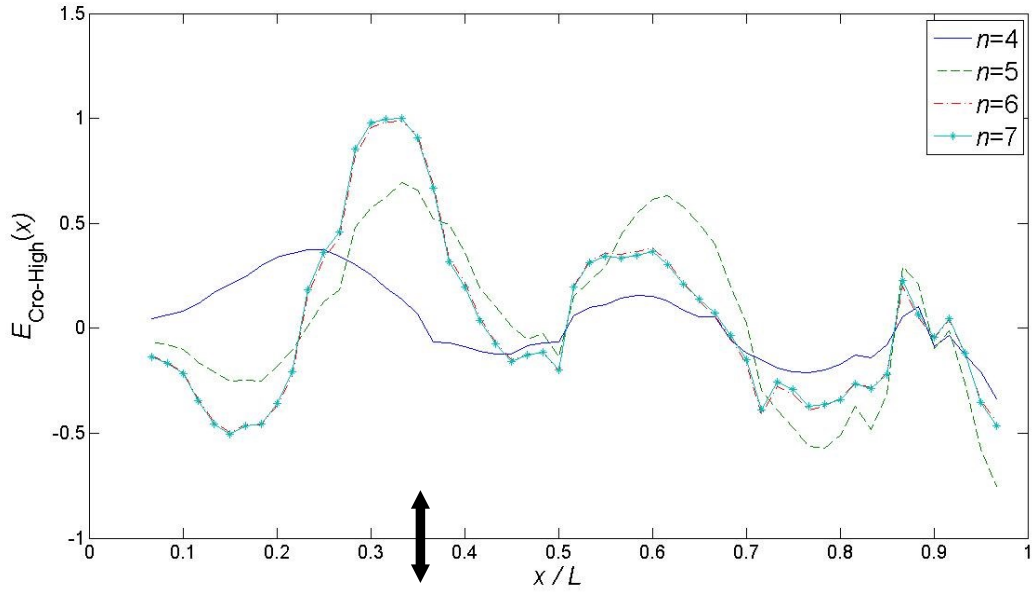
Since the magnitude of the excitation force was not controlled, in order to compare the values with those in numerical solution and numerical experiment, the modal ratio coefficients are normalized by η_1 , so that the proportion of each coefficients can be compared. The normalized modal ratio coefficients are shown in Table 4.5.

By using Eq. (2.29), the FLI was calculated, where α was 1. The result is shown in Fig. 4.19. The FLI after noise reduction is shown in Fig. 4.20.

Table 4.5 Normalized modal ratio coefficients in experimental test, numerical experiment and numerical solution (fixed-free boundary condition)

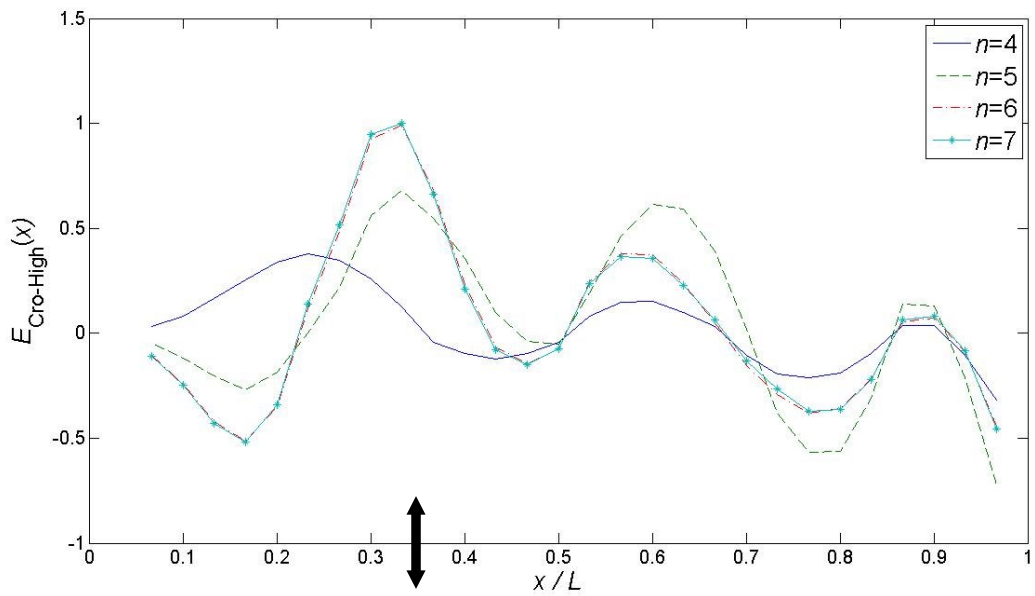
Order	η_r (ET)	η_r (NE)	η_r (NS)
1	1	1	1
2	-1.3849	-1.3764	-1.3765
3	-0.1532	-0.1411	-0.1414
4	0.0072	-0.0036	-0.0034
5	-0.0130	0.0117	0.0113
6	0.0076	0.0051	0.0051
7	5.0409e-4	-3.8231e-4	-2.4328e-4

*ET: Experimental Test; NE: Numerical Experiment; NS: Numerical Solution.



* This figure is normalized through division by the maximum value.

Figure 4.19 FLI calculated in experimental test (fixed-free boundary condition, $x_f = 0.35L$, $\omega_f = 300\pi$ rad/s and $\alpha = 1$)



* This figure is normalized through division by the maximum value.

Figure 4.20 FLI calculated in experimental test after noise reduction (fixed-free boundary condition, $x_f = 0.35L$, $\omega_f = 300\pi$ rad/s and $\alpha = 1$)

Experimental test is to investigate the application of cross-modal energy method under experimental environment to localize the exciting harmonic force.

Table 4.3 and Fig. 4.17 show the measured natural frequencies and mode shapes with their theoretical values. Although it is necessary to point out that the set-up of experimental test can be different from theoretical model, the results still imply a trend that more errors occur in the measurement of higher order modes.

As analyzed in numerical experiment, averaging is effective to handle the influence of noise on the calculation of modal ratio coefficient. According to Fig. 4.11 and Fig. 4.12, the 500-times averaging largely reduced the random noise and produced smooth measured mode shapes and operational response. Table 4.5 shows the normalized modal ratio coefficients calculated from the well averaged mode shapes and operational response. It can be found that the proportion of coefficients, which decides the location, is almost the same as that in numerical solution and numerical experiment except for the 7th modal ratio coefficient. This verifies the prediction in numerical experiment that just enough averaging can satisfactorily handle the problem caused by random noise in calculating modal ratio coefficient.

Fig. 4.19 depicts the FLI calculated based on the measurement. Although

with the noise in cross-modal energy density elements, the FLI still indicates possible location of external exciting force at about $0.325L$, which is slightly different from real location $0.35L$. Fig. 3.20 gives the result after reducing the noise in cross-modal energy density elements. This improved FLI shows a better indication of the location of exciting force. By comparing the FLI in Fig. 4.19 and Fig. 4.20, it could also be illustrated that the amplification of noise caused by the derivative in cross-modal energy density element has limited effect on the accuracy of FLI.

The reason for the slight difference between the identified location and real location may be mainly attributed to the random noise and the connection between excitation and beam. The influence of noise has been shown in Table 4.5. For the connection, as illustrated in Fig. 4.14, the excitation force was connected with beam through a force transducer. The noticeable size of transducer, which is about 0.01 m, can make the real location a bit different from $0.35L$.

4.4 Summary

In this chapter, LSM was applied to reduce the influence of noise caused by the ill-condition of inverse problem in cross-modal energy method. The influence of noise in measurement can be shown in obtaining modal ratio coefficient and cross-modal energy density element. The results of

numerical experiment suggest that the influence of noise on modal ratio coefficients can be controlled just by enough averaging and the errors in obtaining modal ratio coefficients do not affect the location prediction seriously. On the other hand, the amplified noise caused by the derivative in cross-modal energy density element has limited effect on the accuracy of FLI. And, since cross-modal energy density element does not contain the information of the location of exciting force, the noise in cross-modal energy density element may be reduced without using carefully-designed filter. The cross-modal energy method was successfully verified by experimental test.

Chapter 5 Conclusions and Suggestions for Future Work

This chapter concludes the major findings in this research, mentions the limitations and proposes the suggestions.

5.1 Conclusions

This research shows that mechanical vibration energy can be decomposed into two parts: diagonal-modal energy density and cross-modal energy density. The diagonal-modal energy density represents the modal energy distribution, while the cross-modal energy density shows the energy shift caused by external exciting force.

As stated in the Section 1.2, the previous study about energy decomposition is limited. The energy decomposition based on the vibration modes and its physical meaning were first studied in this research. The cross-modal energy density represents the effect of external exciting force on the energy distribution.

It is also found that the summation of high order cross-modal energy terms shows an accumulation phenomenon at the location of exciting force. A FLI is constructed based on the discovery of this accumulation phenomenon. Both numerical and experimental tests are carried out to test the effectiveness of the proposed FLI for force localization.

As mentioned in Section 1.1, the amplification of noise caused by high order derivative occurs in other force identification methods including FAT and the power flow method. The proposed force localization method does not depend on the derivative of the vibration signal. Therefore, the proposed method may have the ability to cope with higher signal to noise ratios than FAT and the power flow methods.

5.2 Limitations and suggestions for future work

There are a few limitations in this research. One is that a more generalized model for the structure and excitation should be applied to examine the proposed method. Another one is that the study of the influence of noise needs further theoretical analysis about the least number of measured points and comparison with other methods..

In order to generalize the model, there are three possible improvements. A plate model can be applied. And, it is also possible to examine the proposed method under non-uniform beam model. A further study can be conducted on the situation for multiple force excitation.

In order to further investigate the influence of noise, there are two possible methods. The first one is to study the relationship between the number of measured points and the influence of noise. The other one is to compare the effectiveness of proposed method with other force identification methods.

Appendix A

Extraction of amplification coefficients through Least Squares Method

In the numerical experiment and experimental test, the operational response and mode shapes are measured at a finite number of discrete points. Eq. (2.5), thus, can be rewritten by the measured values

$$\mathbf{w}(x) = [\mathbf{W}_1(x) \quad \mathbf{W}_2(x) \quad \cdots \quad \mathbf{W}_n(x)] \cdot \boldsymbol{\eta} = \mathbf{W} \cdot \boldsymbol{\eta} \quad (\text{A.1})$$

where $\mathbf{w}(x)$ and $\mathbf{W}_x(x)$ are both $m \times 1$ matrixes. Here, m is the number of measured points and n is the number of included modes. The truncation error is neglected.

In order to minimize difference between the extracted coefficients and the theoretical ones, the LSM is applied to obtain the solution. The modal ratio coefficients can be estimated as

$$\boldsymbol{\eta} = (\mathbf{W}^T \mathbf{W})^{-1} \mathbf{W}^T \cdot \mathbf{w}(x). \quad (\text{A.2})$$

The amplification coefficients, then, can be calculated through Eq.

(A.3)

$$\Gamma_{jk} = \eta_j \eta_k \quad (\text{A.3})$$

References

- [1] Bartlett, F.D., Flannelly, W.G., Modal verification of force determination for measuring vibratory loads, *Journal of the American Helicopter Society* 24(2) (1979) 10-18.
- [2] Carniel, X., Otte, D., Made, C., Pascal, J.C., Application of singular value analysis for structure-borne intensity estimation in multivariate vibration environments, *Proceedings of the 19th International seminar on Modal Analysis*, Leuven, 1994.
- [3] Djamaa, M.S., Ouella, N., Pezerat, C., Guyader, J.L., Mechanical radial force identification of a finite cylindrical shell by an inverse method, *Acta Acustica united with Acustica* 92 (2006) 398-405.
- [4] Djamaa, M.S., Ouella, N., Pezerat and C., Guyader, J.L., Reconstruction of a distributed force applied on a thin cylindrical shell by an inverse method and spatial filtering, *Journal of Sound and Vibration* 301(3-5) (2007) 560-575.
- [5] Dobson, B.J. and Rider, E., A review of the indirect calculation of excitation forces from measured structural response data, *Proceedings of the Institution of Mechanical Engineers. Part C: Journal of Mechanical Engineering Science* 204 (1990) 69-57.
- [6] Ewins, D.J., *Modal testing: theory, practice and application*, Research Studies Press, 2000.

- [7] Fabunmi, J.A., Effects of structural modes on vibratory force determination by the pseudo-inverse technique, *AIAA Journal* 24(3) (1986) 504-509.
- [8] Fierro, R.D., Golub, G.H., Hansen, P.C. and O'Leary, D.P., Regularization by truncated total least squares, *SIAM Journal on Scientific Computing* 18 (1997) 1223-1241.
- [9] Gavric, L., Darlsson, U. and Feng, L., Measurement of structural intensity using a normal mode approach, *Journal of Sound and Vibration* 206(1) (1997) 87-101.
- [10] Gavric, L. and Pavic, G., A finite element method for computation of structural intensity by the normal mode approach, *Journal of Sound and Vibration* 164(1) (1993) 29-43.
- [11] Giansante, N., Jones, R. and Calapodas, N.J., Determination of in-flight helicopter loads, *Journal of the American Helicopter Society* 27(3) (1983) 58-64.
- [12] Hambric, S.A., Power flow and mechanical intensity calculations in structural finite element analysis, *Journal of Vibration and Acoustics* 112(4) (1990) 542-549.
- [13] Hu, S.L., Wang, S. and Li, H., Cross-modal strain energy method for estimating damage severity, *ASCE Journal of Engineering Mechanics* 132(4) (2006) 429-437.

- [14] Janssens, M.H.A. and Verheij, J.W., A pseudo-force methodology to be used in characterization of structure-borne sound sources, *Applied Acoustics* 61 (2000) 285-308.
- [15] Janssens, M.H.A., Verheij, J.W. and Loyau, T., Experimental example of the pseudo-forces method used in characterization of a structure-borne sound source, *Applied Acoustics* 63 (2002) 9-34.
- [16] Kadambe, S. and Boudreaux-Bartels, G.F., A comparison of the existence of “cross terms” in the Wigner distribution and the squared magnitude of the wavelet transform and the short time Fourier transform, *IEEE Transactions on Signal Processing* 40(10) (1992) 2498-2517.
- [17] Karlsson, S.E.S., Identification of external structure loads from measured harmonic responses, *Journal of Sound and Vibration* 196 (1) (1996) 59-74.
- [18] Leclere, Q. and Pezerat, C., Vibration source identification using corrected finite difference schemes, *Journal of Sound and Vibration* 331 (2012) 1366-1377.
- [19] Lecoq, D., Pezerat, C., Thomas, J.H. and Bi, W., Identification of the acoustic component in the turbulent boundary layer excitation by the force analysis technique, *Proceedings of the Acoustics 2012 Nantes conference*, Nantes, France, 2012, 1839-1843.

- [20] Lee, H.P., Lim, S.P. and Khun, M.S., Diversion of energy flow near crack tips of a vibrating plate using the structural intensity technique, *Journal of Sound and Vibration* 296 (2006) 602-622.
- [21] Liu, Y. and Shepard, W.S., Dynamic force identification based on enhanced least squares and total least-squares schemes in the frequency domain, *Journal of Sound and Vibration* 282 (2005) 37-60.
- [22] Meirovitch, L., *Fundamentals of vibrations*, McGraw-Hill, Boston, 2001.
- [23] Michaels, J.E. and Pao, Y.H., Determination of dynamic forces from wave motion measurements, *Journal of Applied Mechanics* 53(1) (1986) 61-68.
- [24] Noiseux, D.U., Measurement of power flow in uniform beams and plates, *Journal of the Acoustical Society of America* 47 (1969) 238-247.
- [25] Pavic, G., Measurement of structural borne wave intensity, part I : formulation of the methods, *Journal of the Acoustical Society of America* 49(2) (1976) 221-230.
- [26] Pei, S.C. and Tsai, E.J., Cross-term analysis in the modified instantaneous power spectrum, *IEEE Transactions on Signal Processing* 41(1) (1993) 477-480.
- [27] Pezerat, C. and Guyader, J.L., Two inverse methods for localization of

external sources exciting a beam, *Acta Acustica* 3(1) (1995) 1-10.

- [28] Pezerat, C. and Guyader, J.L., Force analysis technique: reconstruction of force distribution on plates, *Acustica United with Acta Acustica* 86 (2000) 322-332.
- [29] Pezerat, C. and Guyader, J.L., Identification of vibration sources, *Applied Acoustics* 61 (2000) 309-324.
- [30] Pezerat, C., Leclere, Q., Totaro, N. and Pachebat, M., Identification of vibration excitations from acoustic measurements using near field acoustic holography and the force analysis technique, *Journal of Sound and Vibration* 326 (2009) 540-556.
- [31] Renzi, C., Pezerat, C. and Guyader, J.L., Vibratory source identification by using the finite element model of a subdomain of a flexural beam, *Journal of Sound and Vibration* 332 (2013) 545-562.
- [32] Starkey, J.M. and Merrill, G.L., On the ill-conditioned nature of indirect force-measurement techniques, *Journal of Modal Analysis* 4(3) (1989) 103-108.
- [33] Stevens, K.K., Force identification problems — an overview, *Proceedings of the SEM Spring Conference on Experimental Mechanics*, Houston, 1987, 838-844.
- [34] Tse and Sing, F., *Mechanical vibrations: theory and applications*, Prentice Hall, 1978.

- [35] Wang, C.Q., Ong, E.H., Qian, H. and Guo, N.Q., Short communication on the application of B-spline approximation in structural intensity measurement, *Journal of Sound and Vibration* 290 (2006) 508-518.
- [36] Wang, X.Q., Wong, W.O. and Cheng, L., Modal power flow with application to damage detection, *International Journal of Engineering Science* 47 (2009) 512-523.
- [37] Wong, W.O., Wang, X.Q. and Cheng, L., Modal power flow analysis of a damaged plate, *Journal of Sound and Vibration* 320 (2009) 84-100.
- [38] Xu, H., Cheng, L., Su, Z. and Guyader, J.L., Identification of structural damage based on locally perturbed dynamic equilibrium with an application to beam component, *Journal of Sound and Vibration* 330 (2011) 5963-5981.
- [39] Zhang, Y. and Mann III, J.A., Measuring the structural intensity and force distribution in plates, *The Journal of Acoustical Society of America* 99(1) (1996) 345-353.
- [40] Zhang, Y. and Mann III, J.A., Examples of using structural intensity and the force distribution to study vibrating plates, *Journal of the Acoustical Society of America* 99(1) (1996) 354-361.